UNIVERSITY OF OKLAHOMA

GRADUATE COLLEGE

INFLUENCE OF FREESTREAM REYNOLDS NUMBER ON UNSTEADY REFLECTED NORMAL SHOCKWAVE-BOUNDARY LAYER INTERACTIONS IN SHOCK TUBE EXPERIMENTS

A THESIS

SUBMITTED TO THE GRADUATE FACULTY

in partial fulfillment of the requirements for the

Degree of

MASTER OF SCIENCE

By

ADAM BICAK

Norman, Oklahoma

2024

INFLUENCE OF FREESTREAM REYNOLDS NUMBER ON UNSTEADY REFLECTED NORMAL SHOCKWAVE-BOUNDARY LAYER INTERACTIONS IN SHOCK TUBE EXPERIMENTS

A THESIS APPROVED FOR THE

SCHOOL OF AEROSPACE AND MECHANICAL ENGINEERING

BY THE COMMITTEE CONSISTING OF

Dr. Hiroshi Ozawa, Chair

Dr. Ramkumar Parthasarathy

Dr. Prakash Vedula

Dedication

To Mehmet Bicak: my grandfather, role model, and biggest fan

Acknowledgements

I would like to start by extending my gratitude to Dr. Ozawa for his oversight and guidance throughout my time in the laboratory. I am thankful for his patience while I fabricated the test section and for helping show the value of effective research and experimental methods. I am indebted to my fellow members of the High-Speed Aerothermodynamics Laboratory; Michael, Jacob, Nick, and Kosuke – thank you all for the support and feedback during our meetings, and for keeping things fun while at the lab.

I would not have been able to complete the test section construction without the insights and experience of the AME Machine Shop staff. Billy and Greg, thank you both for the numerous conversations and life advice during my time in the shop. To the students who worked in the shop and helped double-check my machining toolpaths: without you all, this thesis would not have been possible.

I have endless gratitude for my family and friends, who cheered me on throughout every step of this process and put up with my spontaneous phone calls when I found something new in my data or completed a tricky portion of data analysis. I am deeply thankful to have each one of you on my team! Lastly, I must give a special thanks to my fiancée for being by my side at all points of this journey. Breanna, thank you so much for being patient with me through the countless days and long nights I spent on campus working on my research. I love you!

Table of Contents

List of Figures

List of Tables

Abstract

Shockwaves can sharply increase the temperature and pressure of a gas in a reliable and near-instantaneous manner, leading to their utility of producing desirable conditions for the study of chemical combustion and high-speed gas dynamics. Shock tubes effectively produce regions of high-pressure, high-temperature gas by generating shockwaves that reflect off of the end of the driven section and form a reflected shockwave. Though the flow conditions after this sequence are typically assumed to be steady, phenomena such as the growth and interaction of the boundary layer with the reflected shockwave cause non-ideal fluctuations in these parameters. The effect of the Reynolds number of the flow behind the incident shockwave on these flow phenomena was studied using a newly built test section added to the shock tube facility of the High-Speed Aerothermodynamics Laboratory at the University of Oklahoma. High-speed schlieren imaging and pointwise pressure measurements were used to assess the reflected normal shockwave/boundary layer interaction (SBLI) and pressure fluctuations present in the flow. It was found that increasing the freestream Reynolds number helped decrease the size of the shockwave bifurcation formed from the SBLI while also reducing the amount of pressure fluctuations in the region behind the reflected shockwave. These trends persisted across experiments performed at three distinct shock Mach numbers.

Chapter 1: Introduction

1.1: Shockwaves

When objects or other disturbances pass through a gas, their influence on the gas appears as a series of pressure waves that travel outward at the speed of sound and serve to communicate the presence of the object to the surrounding gas molecules. In cases where the object travels faster than the local speed of sound, these pressure waves coalesce into a single front known as a shockwave. Rather than the smooth fluctuations in thermodynamic parameters typically seen across ordinary pressure waves, shockwaves abruptly and significantly alter the properties of the gas as it is processed. The amount in which these parameters are impacted is largely dependent on the velocity of the shockwave relative to the local speed of sound, known as the Mach number; shockwaves at a greater Mach number will more severely alter the properties of the gas. These shockwaves can either form by an object travelling faster than the speed of sound of the gas, or by the gas itself travelling at speeds in excess of its own speed of sound.

1.2: The Shock Tube

Many research fields make use of specialized, purpose-built laboratory equipment that enable researchers to effectively investigate phenomena of interest to them. Examples include the magnetic resonance imaging (MRI) machine used for medical imaging, anechoic chambers used for signal isolation, and electron microscopes for material characterization. On the other hand, some instruments serve much more versatile roles, and can be used in multidisciplinary research with minimal changes to the overall design. When new findings are discovered within one discipline using such a device, the implications of the results may find value within the others that also make use of it. One such device exists that has found use throughout a wide number of fields: the shock tube. The shock tube has been instrumental in the fields of wind tunnel testing, computational fluid dynamics, chemical kinetics, metrology, nondestructive testing, and biomedicine [1–6]. Shock tubes are capable of producing numerous phenomena of interest, including shockwaves, supersonic flows, and high temperature/high pressure gases; all of these can be reproduced in a repeatable manner with a high degree of accuracy. It is for this reason that shock tubes have continued to play an important role in these fields for over 70 years.

A simple shock tube is composed of two sections of piping separated by a diaphragm. One section is filled with compressed gas, while the other section is typically brought to a lower pressure. These sections are referred to as the driver and driven sections, respectively. The diaphragm can be ruptured by creating a sufficient pressure ratio across its surface or by physically puncturing it; once this occurs, the high-pressure driver gas is allowed to quickly rush into the driven section. At this moment, two waves originate at the diaphragm and propagate in opposite directions through the shock tube. The wave passing through the driven section is a shock wave—henceforth referred to as the incident shock wave—while the wave in the driver section is an expansion fan. Both waves will process the gases that they travel through, modifying their thermodynamic properties accordingly. As the incident shockwave passes through the test gas in the driven section, it increases the pressure, temperature, and density of the gas. Once it arrives at the end wall of the driven section, it reflects and forms the reflected shockwave. This shock wave travels back through the driven section, further increasing the pressure, temperature and density of the test gas while bringing it to rest.

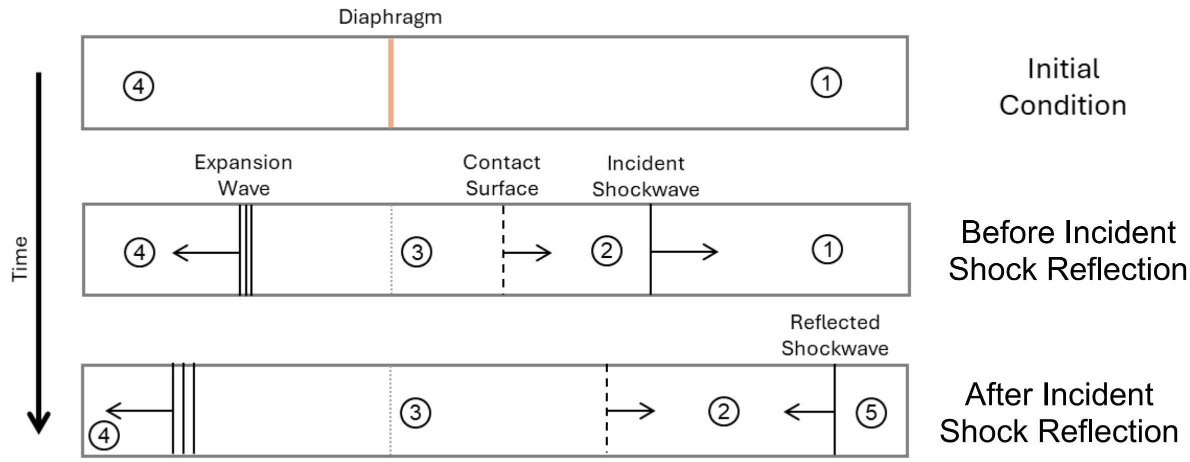

Figure 1. Simplified schematic of the flow structures formed throughout a shock tube experiment

Figure 1 depicts the fundamental flow regions within a shock tube before and after the diaphragm is ruptured. In this case, the initial condition of the driver section is shown as region 4, and the driven section is shown as region 1. The initial conditions of the driver section include the pressure P_4 and temperature T_4; for the driven section, these conditions are denoted P_1 and T_1, respectively. The pressure and temperature in these regions are typically brought to specific values in order to produce desired shock wave speeds once the diaphragm is opened. If the temperature cannot be controlled, then the primary means of modifying the shock speed is by adjusting the pressure ratio across the diaphragm; this ratio is known as P_4/P_1.

Region 2 represents the test gas after it has been processed by the incident shock wave; similarly, region 3 represents the driver gas after it has passed through the expansion fan. Separating regions 2 and 3 is a contact surface; the velocity and pressure are constant across the contact surface, while the temperature and density will vary. Once the incident shockwave reflects off the end wall, the reflected shockwave subsequently passes through the gas in region 2; this ideally brings the gas to rest, while substantially increasing its pressure and temperature. Shown as region 5 in Figure 1, the pressure in this region (P_5) will serve as the primary focus of this thesis.

The reflected shockwave will continue to travel through the driven section until it arrives at the contact surface. The interaction between the reflected shockwave and the contact surface results in a pressure wave that travels back towards the end wall. This pressure wave signals the end of region 5. Alternatively, region 5 can be ended by the propagation of the expansion wave front through the driven gas after its reflection off the endwall of the driven section.

Preliminary analyses using the shock tube typically make the assumption that the flow properties can only vary along the streamwise axis. This dramatically simplifies the calculation of the flow parameters throughout the shock tube and permits use of the Rankine-Hugoniot relations to determine the changes across each shock or expansion wave. If the initial pressures and temperatures within the shock tube and gas species within the driver and driven sections are known, the conditions in regions 1-5 can be found with little trouble. Furthermore, the velocities and Mach numbers of the incident and reflected shock waves can be calculated through this method.

Ideally, the shock Mach number M_s is solely a function of the shock tube pressure ratio P_4/P_1. This relationship is found by one-dimensional shock tube theory and neglects several factors that, in reality, contribute to attenuation of the incident shockwave. For the shock tube facility used in this research, the primary sources of the attenuation are the formation and growth of a boundary layer along the walls of the driven region as well as the usage of a pneumatic fast-opening valve in place of a diaphragm between the driver and driven regions.

The freestream Reynolds number within region 2, or Re_2, is defined as

$$Re_2 = \frac{\rho_2 u_2}{\mu_2} \tag{1}$$

where ρ_2, u_2, and μ_2 represent the density, velocity, and viscosity within region 2. As P_1 and T_1 are typically known quantities, the density in region 1—denoted as ρ_1—can be determined through the ideal gas law. Subsequently, the parameters in region 2 ρ_2, P_2, u_2 and T_2 can be found through the normal shock relations calculated across the incident shockwave using M_s. The region 2 viscosity μ_2 can be approximated using Sutherland's law based on T_2 and the gas species [7]. Through this process, it is seen that Re_2 can be determined if the properties of the incident shockwave and the initial conditions of the shock tube are known. If T_1 does not significantly change and M_s remains constant, then the primary parameter responsible for modifying Re_2 is P_1. This factor is key to the testing procedure used in this thesis.

It is important to note that the variant of Reynolds number used in this case is the *unit* Reynolds number and has units of 1/m (per meter). This definition of Reynolds number is commonly used in wind tunnel nomenclature as a means of describing the capabilities of the testing environment. If the unit Reynolds number of a wind tunnel is known, then the actual Reynolds number of a specific test specimen may be found by multiplying it by the characteristic length scale of the specimen.

1.3: Related Research

It was found that, as a shockwave travels within a duct, a boundary layer forms behind it that grows over time and, depending on the test conditions, may transition from laminar to turbulent before the arrival of the reflected shockwave. This boundary layer introduces nonuniformity into the gas within region 2 and causes measured values to deviate from those found by the one-dimensional assumptions.

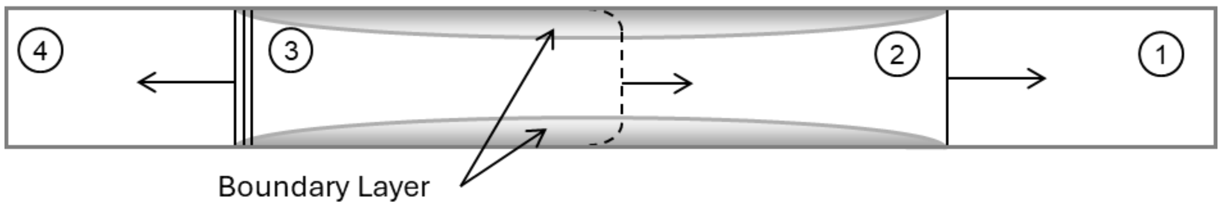

Figure 2. Schematic depicting the development and growth of the boundary layer behind the incident shockwave in a shock tube experiment. Adapted from Mirels [8].

A depiction of the boundary layer formation in regions 2 and 3 can be seen in Figure 2. Mirels documented and found analytical solutions to the growth of the laminar boundary layer formed behind a shockwave within a duct, and later extended these findings to the turbulent case [9,10]. Later, Mirels *et al.* theorized that the formation and growth of the boundary layer causes disturbance waves to propagate throughout regions 2 and 3 [8]. These waves slightly vary the flow conditions within these regions, causing small streamwise perturbations in velocity and pressure. When these waves reach the incident shockwave, it begins to attenuate, and its strength decreases as it continues through the driven section. Rudinger theorized that the small streamwise pressure gradient in region 2 would be magnified behind the reflected shockwave, and performed an analytical study through method of characteristics as well as shock tube experiments to investigate this concept [11]. He found that, as the incident shock strength increased, a measurable pressure rise occurred in region 5. The pressure rise was also found to be higher for experiments in which the boundary layer was primarily turbulent, suggesting an inverse relationship between the pressure rise intensity and the boundary layer thickness.

The pressure rise in region 5 continues to appear as a point of analysis in shock tube studies. Petersen *et al.* found that, through measurement of the pressure growth rate in region 5, isentropic assumptions could be used to estimate the accompanying temperature growth rate; comparison with an analytical reflected-shockwave model showed reasonable accuracy for this approximation

[12]. Hargis *et al.* performed shock tube experiments with different mixtures of test gas to evaluate the effect of the gas composition on the pressure growth rate. Due to each gas species' limitations on the available range of achievable M_s values, they found it difficult to directly form correlations that neglected Mach number effects; with this consideration in mind, the authors found that tests with high levels of CO_2 in the driven section exhibited the most severe pressure growth [13]. The authors found that, in addition to a relationship between the pressure growth and M_s, an inverse relationship was observed between the pressure growth and the freestream Reynolds number. More recently, Nativel *et al.* investigated the effect of the shock tube diameter on the region 5 pressure growth. It was found that shock tubes with smaller diameters are subject to more significant pressure growth due to the size of the boundary layer relative to the duct width [14]. Tests with increased shock Mach numbers also exhibited higher rates of pressure growth.

Figure 3. Mark's experimental visualization of reflected shockwave bifurcation in a shock tube [15].

Mark sought to evaluate the interaction between the boundary layer and the reflected shockwave. He theorized that, when the pressure within boundary layer cannot match the stagnation pressure within region 5, a region of gas from the boundary layer would collect near the edges of the reflected shockwave and grow as it travels back through the shock tube. After capturing images of the reflected shockwave generated through a series of experiments in a shock tube, he found that the shock structure was non-planar and split into a series of oblique waves near the walls, which is now referred to as shockwave bifurcation [15].

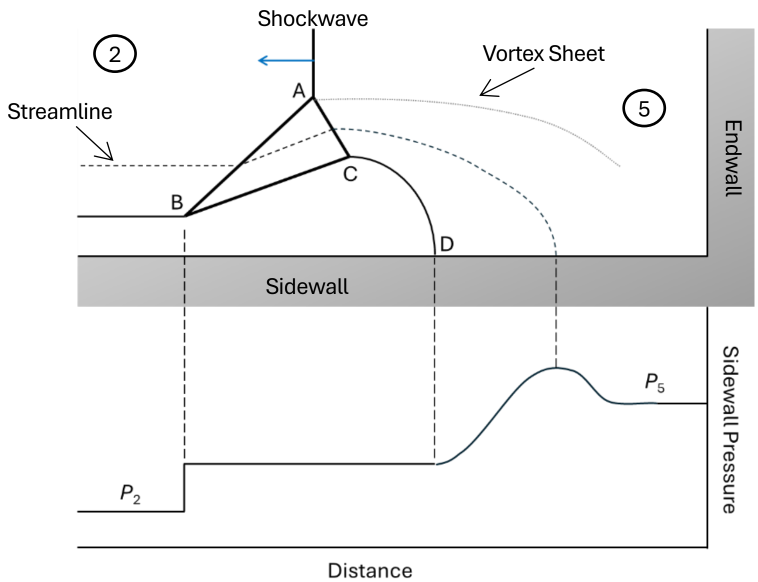

Figure 4. Schematic of reflected-shock bifurcation and its influence on sidewall pressure measurements taken throughout its passage.

A schematic of the idealized bifurcation structure and its effect on the sidewall pressure is shown in Figure 4 and is based on Petersen and Hanson's model, which itself was modified from Mark's original observations [16]. Letters A-D correspond to the key features of the bifurcation structure. The point where the normal reflected shockwave splits into the bifurcation is known as the "triple point" and is denoted by A. The leading oblique shockwave is shown by line AB, where B is the point at which the oblique shockwave terminates within the boundary layer. After point B, the energy-deficient boundary layer underneath the bifurcation separates from the sidewall and forms a recirculation region underneath and behind the bifurcation. The second shockwave AC causes the flow direction to return to initially be parallel with the wall. After point D, the boundary layer is assumed to reattach to the wall, causing a stagnation streamline to exist that eventually impinges upon the sidewall.

Later, Davies and Wilson found that the height of the bifurcation was roughly proportional to the distance travelled by the reflected shockwave and was somewhat dependent on the properties of the test gas as well as the incident shock Mach number [17]. Through further experimentation, Matsuo *et al.* determined that, at a certain distance from the end wall, the bifurcation foot height approaches a constant value that is dependent on the incident shock Mach number [18]. This implies that two primary flow regions exist; in the first, an imbalance exists between the momentum of the boundary layer flow and the skin friction induced by the wall in the separated region. Once these approach an equilibrium condition, the bifurcation height stabilizes; this is referred to as the second region in their investigation. Matsuo also found that the velocity of the reflected shockwave decreases in the first flow region before increasing during the transition from the first to the second regions; eventually, the reflected shockwave velocity approaches its initial value. The magnitude of the maximum velocity loss, as well as the stream-wise point at which this occurs, depended on the incident shock Mach number.

The impact of the test gas species on the bifurcation has also been studied. Strehlow *et al.* originally noticed that, when monatomic gases like argon or helium were used as the test gas, little to no bifurcation occurred for M_s up to 5 [19]. Tests using diatomic gases such as nitrogen and oxygen reflected weak bifurcation above $M_s = 1.4$, while triatomic gases resulted in the strongest bifurcations across a larger range of M_s. Petersen *et al.* further pursued this phenomenon and performed additional shock tube testing with numerous mixtures of monatomic and polyatomic test gases, with the mixtures' ratio of specific heats γ ranging from 1.29 to 1.51 [16]. It was found that the height and width of the bifurcation exhibited a strong dependence on γ, and that special care must be taken to account for the test gas species when predicting the conditions in region 5 for chemical kinetics studies. This effect has been shown to make investigations using polyatomic gases difficult, though not impossible, to analyze in practice [13,20].

A significant impact of the reflected shock bifurcation is additional degradation to the homogeneity within region 5. Mark's original bifurcation studies found that the gas that passes through the bifurcation exits with a non-zero streamwise velocity component [15]. This gas becomes trapped behind the bifurcation for some time before dispersing towards the end wall. Davies *et al.* noted that, once the bifurcated shockwave reaches the contact surface, the bifurcation allows cold driver gas to pass through it and travel along the walls of the shock tube [17]. Once this gas reaches the endwall, it is able to contaminate the hot gas in region 5 through mixing and cooling. For shock tubes operating within tailored conditions, this significantly reduces the usable test time within region 5, which can pose problems for reflected-type shock tunnel testing. Kleine *et al.* visualized the arrival of the bifurcation-processed gas at the endwall of a shock tube using Schlieren photography. The gas formed a small vortex in the corner of the endwall and began slowly converging towards the central axis of the tube [21].

Davies and Sanderson found that sidewall pressure measurements of the reflected shock wave included a small 'bump' shortly after the shock wave arrival [17,22]. They determined that the initial pressure rise was caused by the passage of the first shockwave in the bifurcation foot. Eventually, a stagnation streamline from the bifurcation would pass over the sensor, causing the pressure bump seen in their measurements. Wilson *et al.* found that, if the total size of the bifurcation structure was small relative to the size of the pressure sensor, the overshoot was not measurable [23].

The level of higher-frequency disturbances in the shock tube is an additional topic of research. Trolier and Duffy utilized hot-wire anemometry to evaluate density fluctuations ahead of and behind the reflected shock wave [24]. The authors confirmed that turbulence in region 2 was amplified by the reflected shockwave; however, the amount of amplification was reduced if Re_2 was increased. Similar findings were obtained by Keller and Merzkirch using a speckle photographic method [25].

1.4: Motivation

The goals of this thesis are to investigate the influence of Re_2 on the range of non-ideal flow characteristics observed in region 5 of a shock tube facility. Applications of shock tubes in which these non-ideal effects have a significant impact include reflected-type shock tunnels and chemical kinetics experiments.

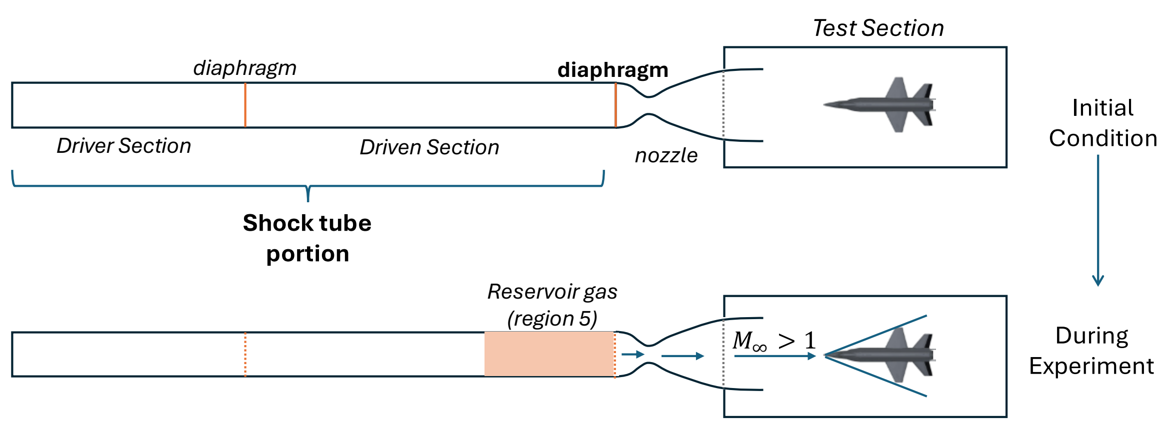

Figure 5. Simplified schematic of a reflected-type shock tunnel facility (not to scale)

Reflected-type shock tunnels combine a traditional shock tube with a converging-diverging nozzle to produce supersonic or hypersonic flows; an example layout of a shock tunnel is shown in Figure 5. The endwall typically found at the end of the driven section in the shock tube region is replaced with an additional diaphragm that separates it from the nozzle inlet. When the incident shockwave reflects off the second diaphragm, the reflected shockwave is generated and forms region 5. In this case, the elevated temperature and pressure in region 5 cause the diaphragm to rupture, causing the gas in this region to quickly enter and accelerate through the nozzle. The gas in region 5 serves as the reservoir to the nozzle; therefore, if the pressure or temperature in region 5 changes over time, then some of the conditions downstream of the nozzle will also experience changes that may dramatically impact the flow quality. This includes the level of freestream turbulence and Reynolds number of the flow. For example, if the downstream Reynolds number begins to fluctuate due to changing conditions upstream, then the location of boundary layer transition on a test model may vary, which can significantly alter the amount of aerodynamic heating experienced during high-speed experiments [26]. Furthermore, any freestream turbulence present in the reservoir will be transported downstream, making the production of quiet freestream flow difficult to achieve. Since the shock tube used in shock tunnels features an additional diaphragm in place of a traditional endwall, endwall-based measurements cannot be taken *in situ* to document the flow quality in the reservoir; rather, measurements taken along the sidewalls serve as the primary means of surveying the reservoir conditions. The unique ability of the shock tube to take measurements at the endwall allow for trends to be found between a test's initial conditions and the resulting amount of freestream noise or pressure fluctuations in the reservoir, which could be applied to shock tunnel experiments in the future. For these reasons, the amount of fluctuation in the reservoir should at least be characterized to some extent to help quantify the level of fluctuation in the freestream flow.

Some laboratories use the near-instantaneous changes in pressure formed by a shock tube to dynamically calibrate pressure sensors; by measuring the change in pressure across the shockwave and the associated reaction time of the pressure sensor, its response can be linked to the pressure within the tube with a high degree of accuracy [27]. Any deviations in the expected pressure change across the shockwave will impact the quality of the calibration. As such, the findings of this thesis may assist in characterizing the non-ideal flow behavior so that it may be taken into consideration throughout the calibration process.

For those studying chemical kinetics, the shock tube continues to serve as a reliable method to rapidly produce a volume of gas at high pressure and temperature to recreate a combustion environment, such as the combustion chamber in gas-turbine engines. Shock tubes used for this purpose may use fuel injection sprayers to produce a air-fuel mixture in the region 5 gas, which would promptly combust and produce products of combustion or form equilibrium/dissociation reactions. Hong *et al.* noted that even modest pressure or temperature growth in region 5 was able to noticeably influence ignition delay times for H_2-O_2-Ar mixtures [28]. Petersen and Hanson similarly found that a change in T_5 of as little as 1% can produce uncertainties exceeding 25% in the dissociation rate coefficients of NO_2 in region 5 [12]. In tests such as these, suppression of the pressure and temperature growth in region 5 is critical to maintain expected testing conditions; in cases where this is not possible, then producing additional data correlating pressure growth with certain test conditions in the shock tube may allow for more accurate models to be produced that could account for these non-ideal effects.

Much of the previous work on this topic has been performed in shock tubes with circular cross sections; the shock tube facility used in this study has a square cross-section, which will allow for any findings to be applicable to other researchers who also use shock tubes with such configurations. It has already been found that shock tubes with a rectangular cross-section possess a different spanwise boundary-layer profile than their circular counterparts [29]. If the condition of the boundary layer is a primary factor in the non-ideal effects seen in the shock tube, then it is reasonable to assume that the results in a shock tube with a square cross-section may differ from previous findings.

The shock tube facility used in this study also has the distinct advantage of using a fast-opening valve in lieu of a traditional diaphragm to separate the driver and driven sections. A primary advantage of this inclusion is the ability to run a series of experiments at the same desired testing conditions with little to no variation between tests. Once a specific combination of P_4 and P_1 values has been found to produce a shock wave with a particular M_s, it can be used repeatedly without fear of run-to-run variations in the results.

Previous research into this topic has included varying attributes such as the test gas composition, P_5, or M_s, for example. Some cases may exist where these attributes cannot be easily modified without other changes to the experimental setup; similarly, some experiments may require these parameters to be fixed. In such a situation, if a minimization of the non-ideal effects is desired, then Re_2 may be one of the only configurable parameters available that do not require significant adjustments to the experimental setup. In these cases, the results of this thesis could serve as a valuable resource for what adjustments could be made to the initial conditions of an experiment. Such adjustments would allow for similar shock speeds and pressure ratios but include a different Re_2.

Chapter 2: Experimental Methods

2.1: Experimental Facility and Setup

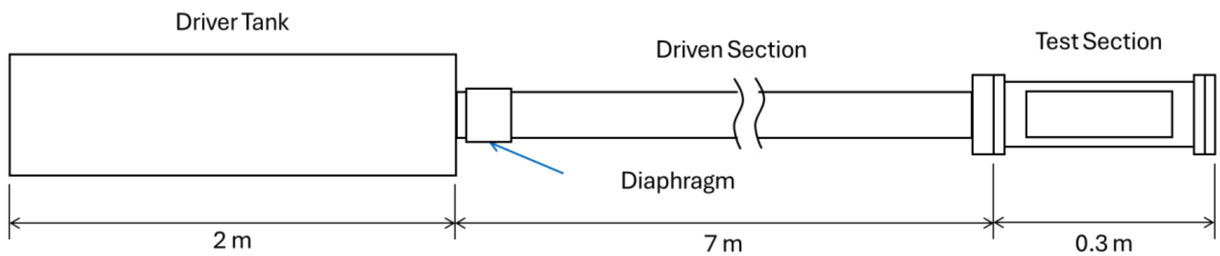

Figure 6. Simplified schematic of the shock tube facility at the High-Speed Aerothermodynamics Laboratory.

The facility used in this study was the shock tube facility at the High-Speed Aerothermodynamics Laboratory at the University of Oklahoma. The shock tube is a monotonic-convergent type; the driver section has a larger internal cross-sectional area than the driven section, which results in stronger shock waves at a given pressure ratio than for shock tubes with a uniform cross-sectional area [30]. The driver section is a 2-meter long cylinder, while the driven section is a 7-meter long rectangular duct with an internal 72-by-72 millimeter cross-section. The corners of the rectangular cross-section are filleted with a radius of 4 mm. A flange at the end of the driven section allows for the installation of a test section or extensions to its length. Between the driver and driven sections lies a pneumatic fast-opening valve from ISTA Pneumatics, which serves as a reusable diaphragm and can be remotely triggered to open and begin a test. The fast valve requires a minimum driver tank pressure of approximately 500 kPa to operate; if the driver pressure is below this value, the fast valve will not open when desired. A general schematic of the facility is shown in Figure 6.

To properly measure the conditions at the endwall and sidewall of the shock tube, a new test section needed to be designed and constructed. The previous test section used with the shock tube featured a change in cross-sectional area and geometry, so the flow would not follow steady assumptions outlined by traditional shock theory. The new test section needed to meet the follow requirements:

- The cross-sectional properties of the driven section of the shock tube must be preserved in the test section design to maintain uniform flow properties behind the incident shockwave.
- The top and bottom walls of the test section must feature modular, replaceable inserts that can accommodate different types of sensors or measurement devices. These inserts should sit flush within the walls of the test section to minimize the creation of perturbations in the flow, which can further attenuate the incident shock wave.
- The sides of the test section must accommodate windows that span from the bottom to the top of the flow region, so that the wall boundary layer may be observed through schlieren imaging or other flow visualization techniques.
- The end wall must extend into the visualization area, so that the moment of incident shock reflection may be captured.
- The test section must be airtight and capable of maintaining strong vacuums for extended periods of time. It must also be able to withstand the elevated pressures and temperatures experienced during testing.

With these requirements established, preliminary designs for the new test section were developed. A 3D model of each component was produced in SOLIDWORKS, with a complete assembly and part drawings developed as well. One of the principal drawbacks of the original design was the need for airtight, smooth welds at multiple locations inside and outside of the test section. These welds would have to have minimal porosity and would thus require validation through X-Ray or other techniques. This would increase the cost of the test section considerably and would result in numerous weak points that could fail over its operational lifetime.

An additional limitation of the original design was the sealing method around the windows. Typical test section windows employ a two-tiered geometry, so that a gasket could be used to provide an airtight seal between the window and the test section body while still allowing for the window surface to sit flush. The first test section design featured non-tiered glass panes, so a traditional flat gasket between the window and the test section could not be used; without any contact between the short ends of the window and the test section, there would be no place for the gasket to be compressed. This prompted several changes from the original conceptual design.

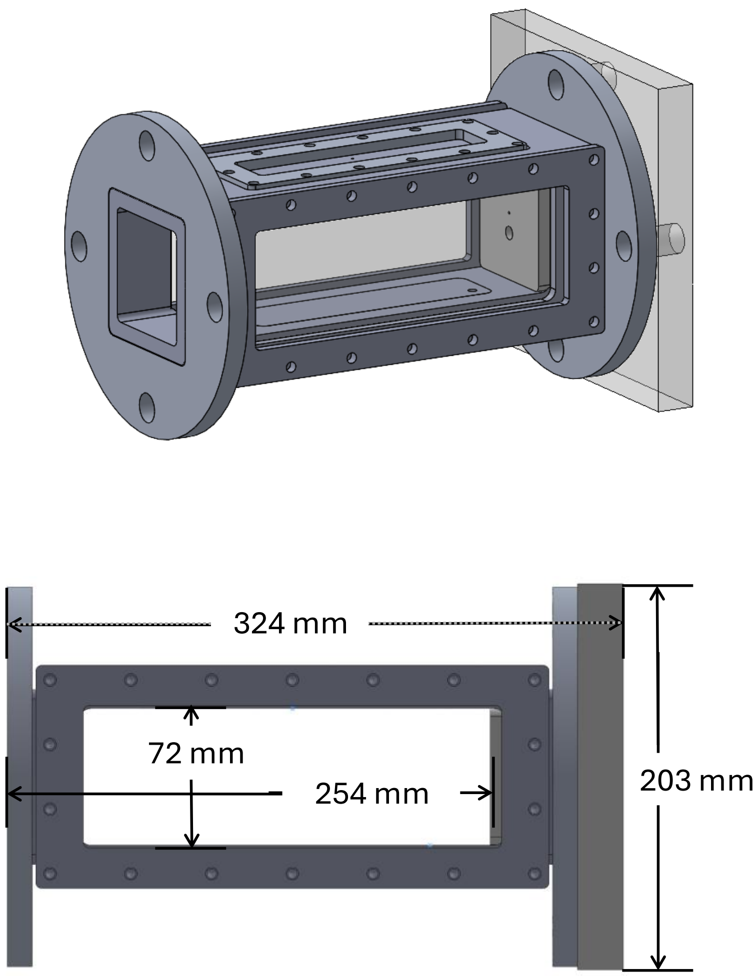

Figure 7. CAD model of the final iteration of the test section assembly used in shock tube experiments. Top: isometric view. Bottom: side view.

The final design of the test section is seen in Figure 7. The body of the test section is composed of a single billet of 6061-T6 aluminum alloy. A solid block of this material was acquired and its corners made square to assist in the manufacturing process. To give it the necessary internal and external geometry, the block was milled using a Haas VF-0E vertical CNC mill. The milling process was extensive, as all six sides of the original stock had to be operated on to produce the hollow interior and geometries to accommodate the windows and wall plates. The wall plates, windows, and end wall were also manufactured through CNC machining. However, the retaining brackets for the windows and wall plates, as well as the mounting flanges for the test section were manufactured by waterjet cutting due to their simple geometry and thin stock size.

Despite the unibody construction of the finalized test section's body, some weldments were still required to complete the final assembly. Specifically, the flanges used to connect the test section to the shock tube would need to be welded onto the body. These welds were located on the outside of the body, so they did not need to be airtight and would not require x-ray inspection. Once the welding was complete and the screw bores were tapped, the test section's interior was sanded before being commissioned into testing.

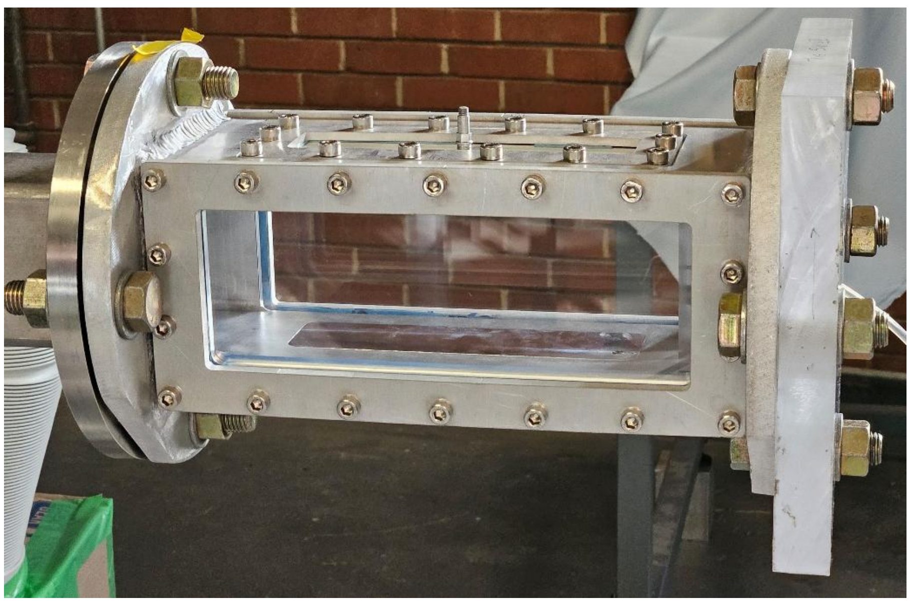

Figure 8. Completed test section installed in the HSAL shock tube facility. The viewpoint is from the left-hand side of the test section.

Figure 8 depicts the fully constructed test section mounted to the end of the shock tube's driven section. The window that would ordinarily be facing the camera is not included in this image to help view the mounting geometry that maintains the airtight seal around the window. The total cost of the test section's creation was $912 USD (including cost of the material, tooling, and weldments). The manufacturing process was performed over the course of roughly six months;

when combined with the time taken to design the test section, the start-to-finish time to ideate and manufacture it was roughly one year.

For this investigation, it was necessary to record the pressure at various points inside the test section during each experiment. To record high-speed pressure measurements, three piezoelectric pressure transducers—hereby referred to as PCB sensors—from PCB Piezotronics were implemented (Model 113B21). These sensors can be mounted through the walls of the shock tube so that the pressure inside the driven section can be measured throughout an experiment.

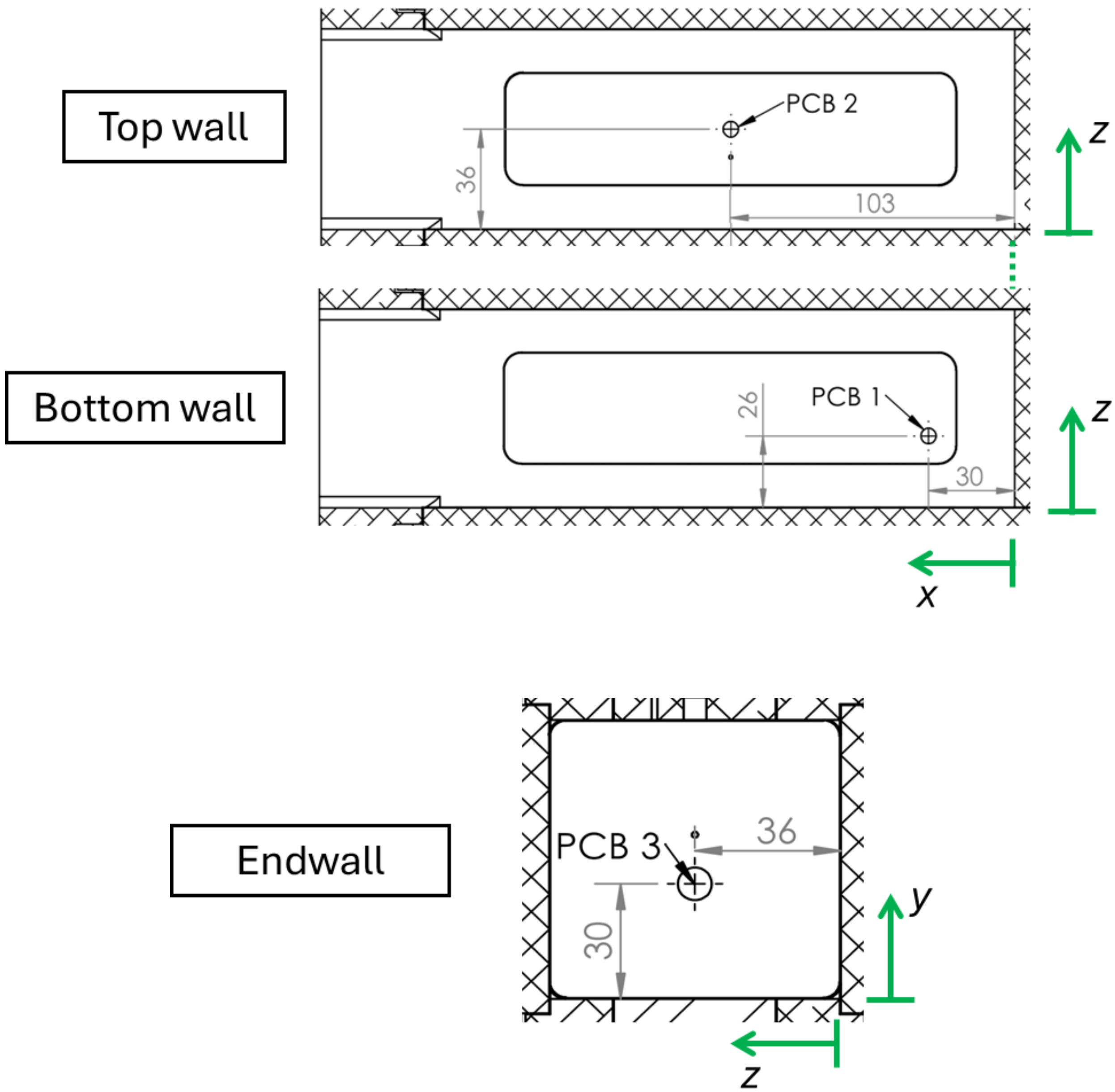

Figure 9. Layout of PCB pressure sensors mounted in the test section of the shock tube. *x, y,* and *z* denote the distances from the endwall, bottom wall, and left-hand window, respectively. Dimensions are in millimeters.

With the configurations made possible with the new test section's removable wall plates, pressure sensors were mounted on the top, bottom, and end wall of the shock tube at the locations shown in Figure 9. While all of the measurement locations will be capable of measuring the pressure in region 5, the top and bottom wall locations will also be able to measure the pressure within region 2; the duration of the region 2 measurement is limited by the time between the passage of the incident and reflected shockwave at the measurement location. For this reason, the pressure sensor on the bottom wall was installed close to the endwall in order to measure a longer duration of region 5 flow, while the top wall pressure sensor was installed further away to provide a usable amount of data in region 2. These two sensors will be referred to as PCB 1 and PCB 2, respectively. The streamwise displacement between the two sensors also allows for measurement of the incident shock velocity. The endwall pressure sensor, referred to as PCB 3, is only capable of measuring the flow within region 5. Figure 9 also highlights the coordinate system used for spatial measurements throughout the analysis; x represents the streamwise distance from the endwall in millimeters, while y represents the distance from the test section's bottom wall in millimeters.

To properly measure the air pressure along walls of the shock tube, it was critical that the circular faces of the pressure sensors were mounted flush to the interior surfaces of the test section. If the sensor faces protruded from the walls or were recessed, the subsequent measurements would not be indicative of the true wall pressure. Rather than directly mount the pressure sensors into the body of the test section, the removable wall inserts were instead machined to accommodate the geometry required for installation of the sensors. After machining the holes for the pressure sensors, the surface of the wall inserts facing the inside of the shock tube were smoothed and polished to remove any burrs or excess material. The endwall's PMMA construction makes installation of threaded objects more difficult than for a metallic material. PCB Piezotronics provides an adapter for their sensors that increases the diameter and thread size necessary for mounting, which allows for stronger and more durable threads. This adapter was used for the pressure sensor mounted in the endwall. All sensors used in this study were connected to a digital data acquisition system from Dewetron and were sampled at 1 MHz.

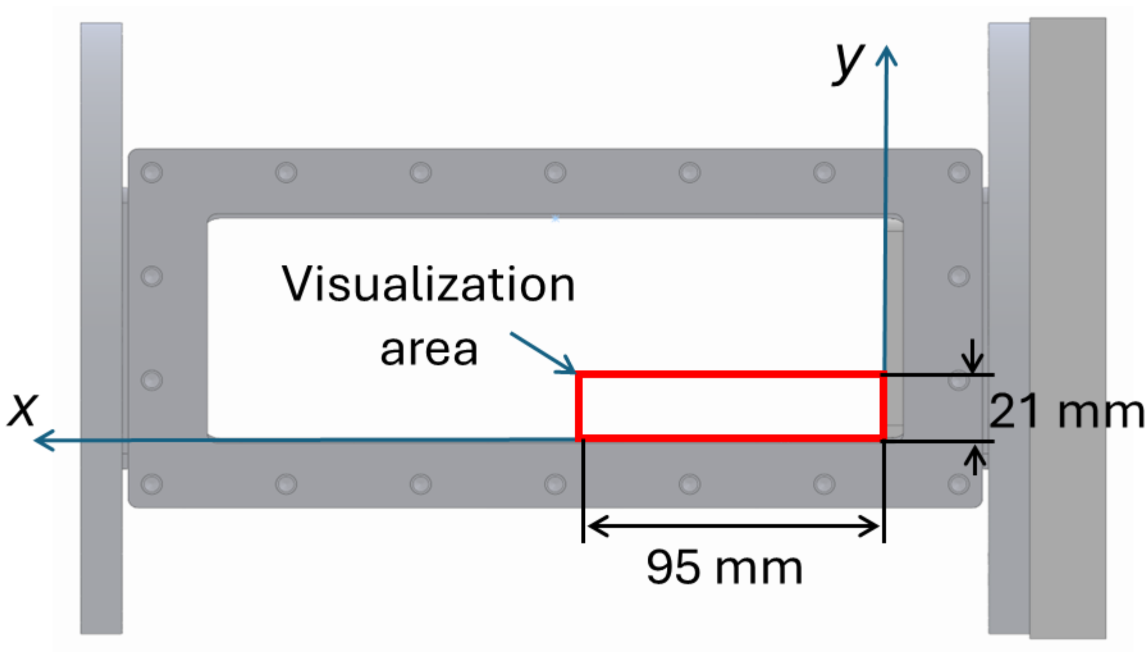

Figure 10. Depiction of the area visualized by the high-speed schlieren setup. The red box shows the field-of-view of the camera. Dimensions are in millimeters.

The characteristics of the boundary layer and bifurcation structure were considered as part of this investigation. Specifically, visualization of the bifurcation and boundary layer formed during experiments was desired. If the boundary layer can be visualized, then its growth over time and subsequent transition to turbulence may also be obtained. Similarly, the temporal changes to the bifurcation structure throughout an experiment may provide insights into its dependence on the initial conditions of the test. To achieve these goals, a high-speed schlieren visualization system was setup. The visualization area of the schlieren setup, shown in Figure 10, was configured to include the flow along the bottom wall of the test section up until the endwall. This area would capture the structure of the incident and reflected shockwaves as well as the density gradients induced by the growth of the boundary layer behind the incident shockwave during tests.

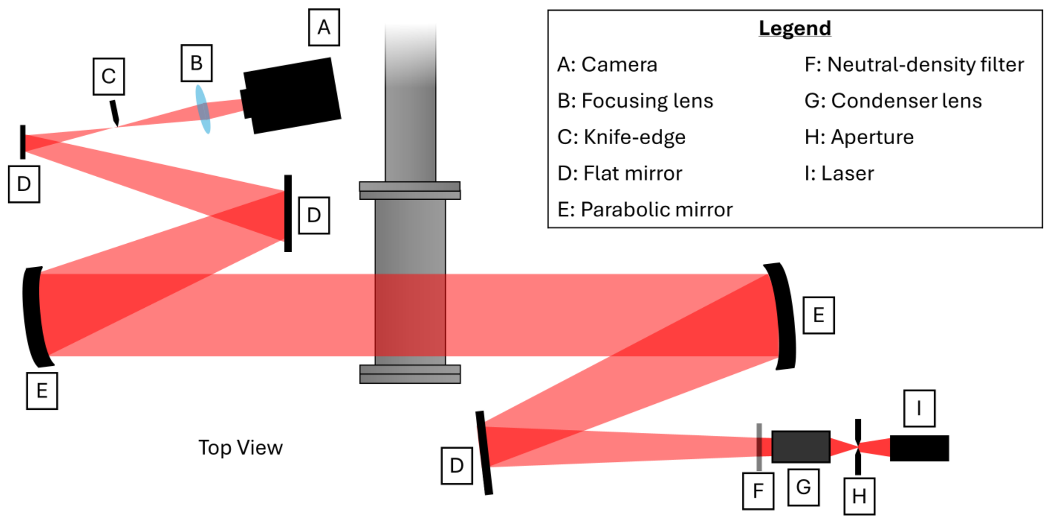

Figure 11. Top-down schematic showing the components used in the Z-type high-speed schlieren imaging system implemented for flow visualization.

A Photron FASTCAM Nova S16 high-speed camera was used to capture the images shown in this study. The light source was a Cavilux pulsed-diode laser system with a pulse width of 10 ns per frame. The laser and high-speed camera were synchronized such that the laser pulses once for each frame that the camera captures; this reduces the motion blur that is associated with a slower shutter speed. The resolution of the images that were captured is 640-by-144 pixels, and the camera's sampling frequency was set to 132 kHz. The camera's exposure time was set to 1.1 µs. The image was focused using an f/200 lens situated in front of the camera sensor. The schlieren effect was produced by cutting the light path's focal point with a scalpel blade, which was positioned such that vertical density gradients in the test section could be visualized during experiments. This setup was maintained throughout all five of the experiments performed with the high-speed camera and is shown in Figure 11.

To trigger the camera, a TTL-signal function generator was connected to the data acquisition system and was set to measure the output voltage of a PCB sensor mounted upstream of the test section. Once the voltage exceeded a threshold value, the function generator would produce a single TTL signal that would be intercepted by the high-speed camera to begin the recording process. After each experiment, the function generator was reset to prepare it for the next test.

The physical dimensions of the flow visualization region were reconstructed by placing a reference object in the test section prior to the experiment and capturing an image of it. For this case, a US penny was used due to its standardized dimensions and convenience. By measuring the diameter of the penny in the vertical and horizontal axis, the relationship between pixel width and linear distance was determined. In this setup, the horizontal and vertical pixel width was found to be 0.15 mm/pixel. This was used to provide the length scales seen in schlieren results shown later in this thesis.

2.2. Testing Strategy

One of the key aspects of this investigation was the goal of keeping the incident shock Mach number constant while varying the freestream Reynolds number across a series of experiments. The method used to vary Re_2 without also varying M_s will now be outlined.

As stated previously, Re_2 is a function of ρ_2, u_2, and μ_2. The freestream velocity u_2 is dependent on M_s and the upstream velocity u_1, which is equal to zero in this case. Therefore, if M_s is held constant across each test condition within a set of tests, then u_2 cannot be adjusted to modify the Reynolds number. The shock tube facility in this study lacks a means of controlling the temperature of the gas within the driver or driven sections prior to each test; for this reason, since T_1 cannot be adjusted, then T_2 cannot be adjusted without also adjusting M_s. This limitation prevents the use of μ_2 in adjusting Re_2. From these limits, the freestream density ρ_2 remains as the only variable that can be adjusted within the operational limitations of the shock tube facility. It is possible that, by adding a temperature control system to the driven section, μ_2 could also be modified in future experiments. The density ratio across a normal shockwave is given by

$$\frac{\rho_2}{\rho_1} = \frac{(\gamma_1 + 1)M_s^2}{(\gamma_1 - 1)M_s^2 + 2} \tag{2}$$

which indicates that, if M_s and γ_1 remain constant, the density ratio will also remain constant and the density in region 2 can be determined. The initial density of the test gas ρ_1 can be determined through perfect gas law:

$$\rho_1 = \frac{P_1}{R_1 T_1} \tag{3}$$

Therefore, to modify Re_2, the initial pressure P_1 can be increased or decreased; this changes ρ_1, which in turn changes ρ_2 and, crucially, Re_2.

The primary goal of this thesis was to examine the shockwave/boundary-layer interaction and non-ideal effects within region 5 across a wide range of Reynolds numbers. To lower the experimental Re_2 value, the initial pressure in the driver and driven sections would be reduced; however, once the driver pressure falls short of the minimum operating pressure of the fast valve, it will no longer function and the shock tube cannot be operated. Conversely, increasing Re_2 requires increasing the driver and driven pressures. In this case, the limiting factor is the maximum allowable pressure in the driver section of the shock tube. Once either of these limits is reached, P_1 cannot be adjusted further without modifying the pressure ratio, which affects the resultant M_s value during the experiment.

The absolute upper and lower limits of the driver pressure in the shock tube are 500 kPa and 700 kPa, respectively. It has also been noted that, when the driver pressure approaches 500 kPa, the opening characteristics of the fast valve changes and some air escapes through the valve before it fully opens. Therefore, a minimum driver pressure of 550 kPa was chosen for this experiment.

A set of five test conditions were proposed for each M_s targeted in this study, and were set by subdividing the driver pressure range into five specific values: 550 kPa, 590 kPa, 630 kPa, 670 kPa, and 700 kPa. These P_4 values are used across all test conditions featured in this study; to vary M_s, P_1 would be adjusted to modify the resultant pressure ratio across the fast valve prior to each experiment.

Fast valves can impose complications when planning which pressure ratios to use to obtain specific test conditions in the shock tube. Amer *et al.* found that the inclusion of a fast valve in a shock tube setup can increase the required P_4 values substantially in order to produce an incident shockwave with a specific Mach number [31], and that the deviation between the experimental and theoretical P_4 values was dependent on the type of fast valve used in addition to the magnitude of P_1 and P_4. This phenomenon has also been observed within the shock tube facility used in this study; for example, a pressure ratio of P_4/P_1 = 600 kPa / 5 kPa = 120 is expected to result in an incident shock wave with Mach number of approximately 2.7. Realistically, pressure ratio has resulted in a M_s of slightly greater than 2.2 when measured at the test section in previous experiments. Of course, the attenuation of the incident shock wave due to unsteady boundary layer growth also contributes to the reduction in the magnitude of M_s, and this must also be considered. Through an application of Mirels' approximations for shock tube attenuation, it was found that a reduction in M_s of only roughly 5% should occur, which results in an attenuated M_s of 2.6 [8]. It was apparent that the fast valve or other facility-dependent features of the shock tube facility were further contributing to the attenuation of the incident shock wave.

To circumvent this problem, an iteration scheme was implemented to determine which combinations of P_4 and P_1 are necessary to produce an incident shockwave with a specific Mach number. The procedure for this iteration was as follows:

1. An initial P_4/P_1 value is estimated. With P_4 fixed, P_1 is chosen such that the pressure ratio is satisfied.
2. The shock tube is brought to the desired initial driver and driven pressures, and a test is conducted.
3. The shock Mach number is measured based on the shock speed u_s and the initial speed of sound of the driven gas a_1.
4. If M_s is too low, then P_1 is decreased. If M_s is too high, then P_1 is increased.
5. A new test is conducted with the modified P_1 value.

This process is repeated for each test condition until the desired shock Mach number is determined. To determine u_s (and, subsequently, the shock Mach number), the pressure recordings taken by the sidewall sensors PCB 2 and PCB 3 are compared.

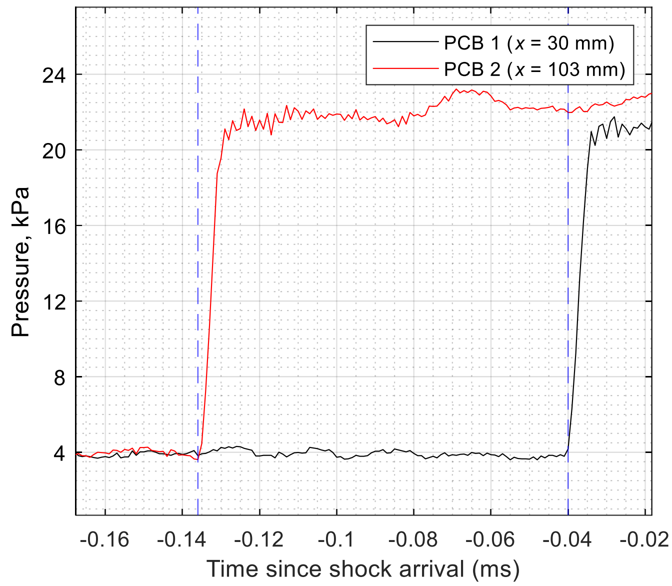

Figure 12. Pressure recordings that captured the passage of the incident shock wave. Dashed lines indicate the moment the incident shock wave passes over each sensor.

Figure 12 shows the step-like pressure rise induced by the incident shockwave as it passed over PCB 2 and, eventually, PCB 1 during a typical shock tube experiment. The time since incident shock reflection t is shown on the horizontal axis, while the measured pressure P is shown on the vertical axis. The time between these two steps is found by determining the point in each signal where the pressure increases by more than 0.5 kPa/μs; the point at which this occurs is shown by the dashed lines. In this example, the time taken for the shock wave to travel from PCB 2 to PCB 1 is 96 μs. The center-to-center distance between the two PCB sensors is known to be 73 mm; therefore, by dividing the travel distance by the time taken, u_s is approximately 760 m/s. Dividing u_s by the speed of sound in region 1 yields an incident shock Mach number of 2.2. This procedure was performed for every test conducted in this study to verify that the desired M_s value was realized. The finalized initial pressures used for each test condition and their corresponding results for M_s and Re_2 are shown in Table 1. An example of the start-to-finish calculation of M_s and Re_2 for one of the test conditions can be found in Appendix A.

Table 1. List of test conditions used for data collection of pointwise pressure measurements.

M_s	Test Condition	P_4 (kPa)	P_1 (kPa)	Re_2, 10^6 1/m
2.0	1	550	10.5	**5.3**
	2	590	12.2	**6.2**
	3	630	13.9	**7.0**
	4	670	15.5	**7.7**
	5	700	16.2	**8.0**
2.2	6	550	4.0	**2.4**
	7	590	5.0	**3.0**
	8	630	6.0	**3.6**
	9	670	6.9	**4.2**
	10	700	7.3	**4.4**
2.3	11	550	2.5	**1.7**
	12	590	3.0	**2.0**
	13	630	3.6	**2.4**
	14	670	4.2	**2.8**
	15	700	4.6	**3.0**

Once a valid combination of P_4 and P_1 was found, a set of three tests was conducted at those conditions. This helped investigate the consistency of experiments conducted at a specific Reynolds number. T_1 was measured prior to each experiment to account for changes in the ambient air temperature across the test campaign, though the total observed T_1 range of 24°C to 26°C only marginally affected the test gas' speed of sound and viscosity. With three tests performed at each of the five test conditions chosen to reproduce a specific shock Mach number, a total of fifteen tests were required per Mach number. Subsequently, since three shock Mach numbers were evaluated, then a total of forty-five tests were performed for pressure data acquisition. For depictions of the pressure measurements of themselves, the results of the three repeatability tests for each condition will be averaged into a single curve to reduce the number of curves seen in a specific figure to help identify any trends present in the results.

It is important to note that the shock tube facility used in this thesis does not have temperature control in regions 1 and 4. The gas temperature in these regions is therefore assumed to equal the ambient temperature of the laboratory at the time that each test was conducted. The room temperature is known to fluctuate based on the weather conditions. To minimize the impact of this on the testing, the test campaign was performed over a span of three days. On each day, all tests pertaining to a specific shock Mach number were performed consecutively. After each specific test was performed, the room temperature was recorded and the shock Mach number was individually measured to verify that the target conditions were met. During this time, the shock tube was given sufficient time for the wall temperature to equalize with the ambient temperature. During the days in which the testing was performed, the room temperature varied by less than 2°C from the start to end of each day, so the subsequent fluctuations in the gas' speed of sound were relatively small.

The test conditions used for the experiments with high-speed schlieren data are slightly different than those used to obtain pressure recordings; this data was obtained earlier in the research process, and the pre-selected values for P_4 had not yet been specified. The nominal M_s for these tests was 2.2, and the corresponding test conditions are shown in Table 2.

Table 2. Test conditions used for collection of high-speed schlieren images.

M_s	Test Condition	P_4 (kPa)	P_1 (kPa)	Re_2, 10^6 1/m
2.2	S1	550	4.2	2.5
	S2	560	4.4	2.7
	S3	590	5.0	3.0
	S4	630	6.0	3.6
	S5	680	7.0	4.3

Chapter 3: Results

3.1. High-Speed Schlieren

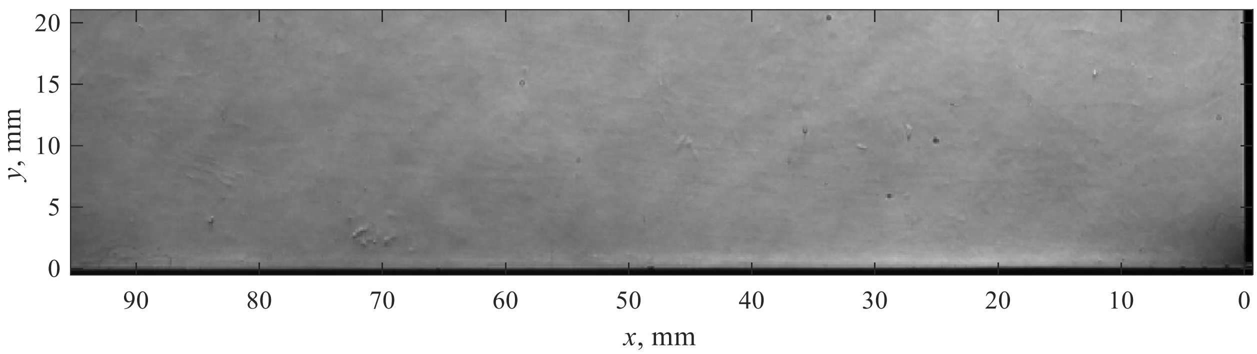

Figure 13. Visible area within the test section visualized by the high-speed schlieren setup prior to the beginning of an experiment.

Schlieren images were captured for the test conditions provided earlier in Table 2. Once recorded, the images were converted into TIFF files and imported into MATLAB for data processing. Even after cleaning the windows of the test section, some small marks and blemishes remained on the viewing surfaces and are visible in Figure 13. Furthermore, the acrylic material used to produce the windows is not fully optically transparent, and some light from the laser is refracted slightly after passing through both windows on the test section. This is most evident in the bottom-right corner of the viewing area, where a minor intensity gradient is visible that causes the region to appear darker. To improve the quality of the images, intensity normalization was implemented. By dividing the intensity I of each pixel within an image series by its original value before the beginning of the experiment I_{ref}, the resulting ratios I/I_{ref} can be used instead; if I/I_{ref} is greater than 1, then the intensity at that location is greater than it was before the beginning of the test, with the opposite holding true for values less than 1. A result of intensity normalization is the diminishing effect of blemishes on the windows and a more consistent image quality.

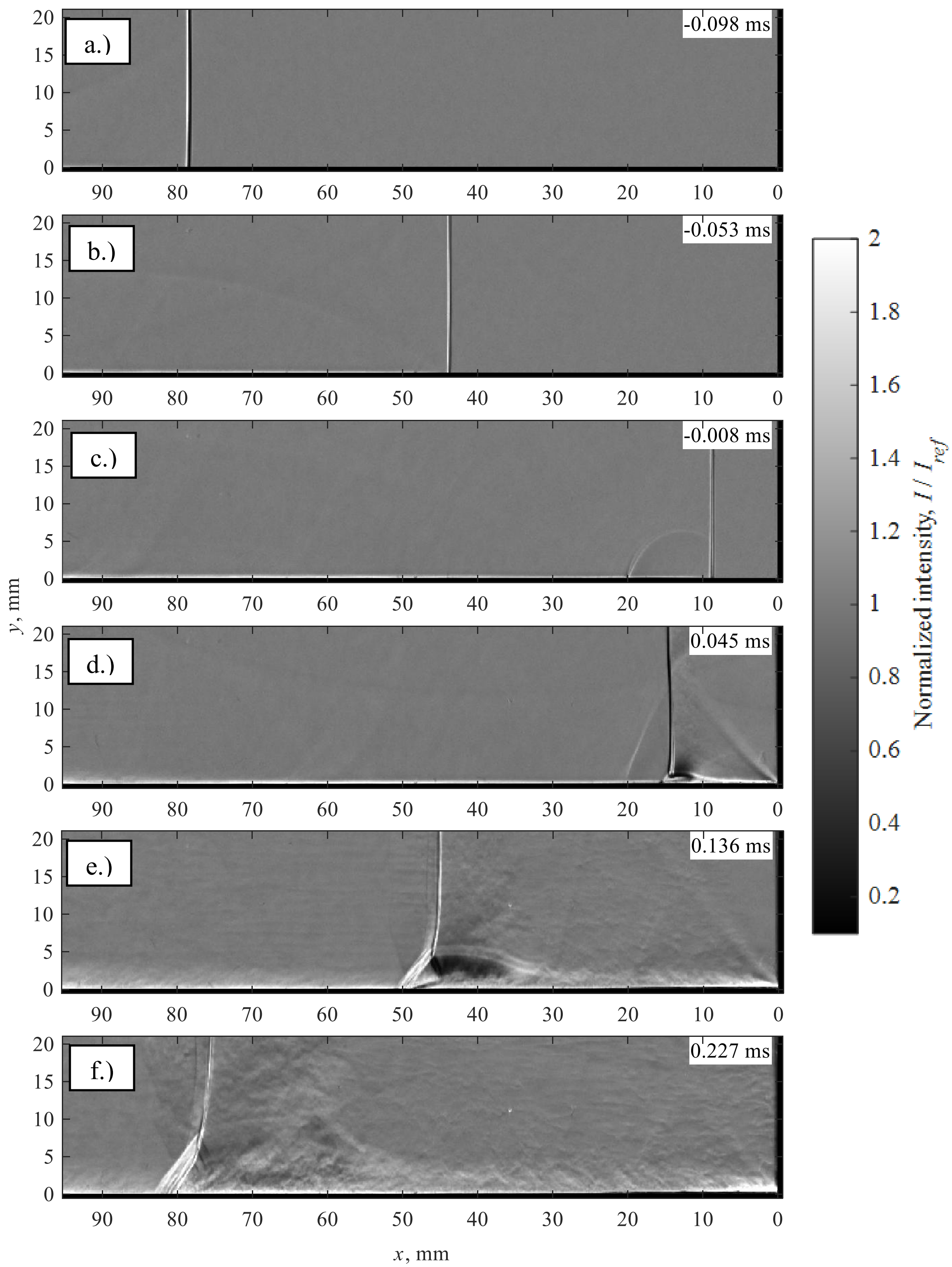

Figure 14. Time series of high-speed normalized schlieren images depicting the incident and reflected shockwaves near the endwall of the shock tube. $Re_2 = 2.5 \times 10^6$ 1/m.

A representative timed series of high-speed schlieren images is shown in Figure 14 corresponding to $Re_2 = 2.5 \times 10^6$ 1/m. The incident shockwave, visualized in the first three images, is seen travelling from left to right towards the endwall. Its shape remained planar throughout the test duration, with no deformation or curvature near the walls of the shock tube. Behind the incident shockwave, a thin line of brighter pixels can be seen along the bottom wall. This density gradient is caused by the formation of a boundary layer that begins to generate immediately behind the incident shockwave and grows until its eventual interaction with the reflected shockwave.

In Figure 14c, a small perturbation in the flow along the bottom wall can be seen near x = 20 mm. This is caused by the small gap between the body of the test section and the removable wall insert; such a gap is unavoidable if the wall plate is to remain removable. It is assumed that similar perturbations are formed at the leading edge of the wall insert as well, though this cannot be confirmed with the current viewing area. Though their presence is not expected to make a significant impact on the results of this thesis, documentation of their existence must be noted in an effort to identify methods of improving the quality of the test section for future experiments.

The images shown in Figure 14d-f captured the passage of the reflected shockwave through the gas in region 2. A bifurcation is clearly visible at the intersection of the reflected shockwave and the bottom wall of the test section. While starting as a somewhat small flow structure, the bifurcation appears to grow in size as the shockwave travels downstream.

In Figure 14d, the overall bifurcation structure is quite small and difficult to deconstruct due to the limited image resolution, while the bifurcation structure visualized in Figure 14e appears to closely match previous visualizations by Mark with a distinct series of shock waves in addition to a slip line and bubble. By the time the reflected shockwave is visualized in Figure 14f, the bifurcation has continued to grow in size; at this point, while the foot shock is still visible, the other components of the bifurcation are not identifiable.

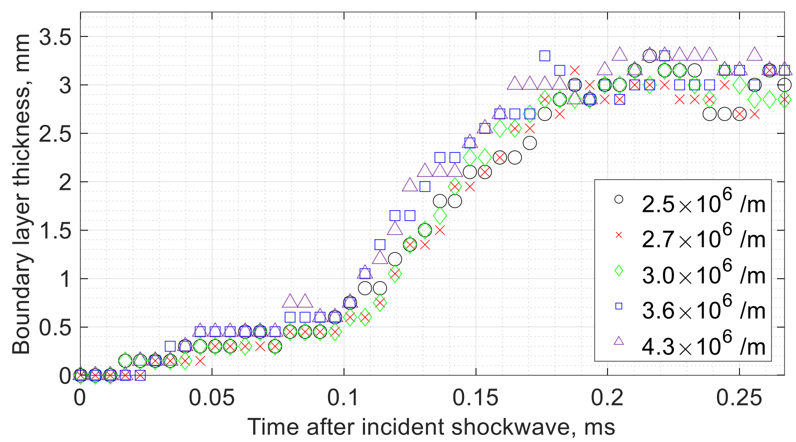

Figure 15. Boundary layer profiles in region 2 at *x* = 90 mm for all schlieren test conditions.

An attempt was made to determine the boundary layer growth behind the incident shockwave seen in the high-speed schlieren images; specifically, the growth of the boundary layer at a specific distance from the endwall was investigated. In this case, a distance of 90 mm from the endwall was chosen. This location experiences a longer span of time between the arrival of the incident shockwave and the reflected shockwave than those closer to the endwall. This improves the likelihood of visualization of the boundary layer transition at this location.

To determine the actual thickness of the boundary layer at this location, variations in intensity along the pixels corresponding to x = 90 mm were evaluated. The schlieren images indicate a noticeable increase in pixel intensity along the endwall, which corresponds to the changes in density induced by the boundary layer. By calculating the normalized intensity at this location and comparing the results to a threshold value, the boundary layer thickness can be defined as the point at which the normalized intensity becomes greater than the threshold [32]. In this case, a threshold value of 1.1 was chosen, meaning that a pixel containing a normalized intensity of greater than 1.1 corresponds to the thickness of the boundary layer at that location. To minimize the effect of camera noise on the result, the vertical intensity data between x = 88 – 92 mm was along the x-axis to obtain a single, averaged column of data at x = 90 mm.

The resulting boundary layer thickness at x = 90 shown in Figure 15. To compare the experimental results with theoretical expectations, the compressible laminar boundary layer equations presented by Mirels were evaluated [9]. Solving this system of equations required some assumptions; the wall temperature was assumed to equal the initial driven gas temperature, and the Prandtl number of the region 2 gas was set equal to 0.72. Calculation of the theoretical boundary layer profile, as well as comparison between the theoretical and experimental boundary layer profiles for a given experiment, are provided in Appendix B.

Initially, the experimental and theoretical boundary layer profiles appear to show a strong agreement. Approximately 0.1 ms after the incident shockwave passed x = 90 mm, the experimental boundary layer thickness begins to rapidly increase from 1 mm to 3 mm before stabilizing for the duration of the region 2 flow. This is caused by the transition of the boundary layer from laminar to turbulent. The boundary layer is likely still thickening at this point; the flattening of the thickness profile may be a by-product of the chosen intensity threshold. While decreasing the threshold may yield more accurate estimations of the boundary layer thickness at some points, the increased sensitivity to noise in the camera data causes sizeable fluctuations in the thickness profile that are not caused by fluid phenomena.

The experimental boundary layer profiles were determined for all five tests that utilized high-speed schlieren and are shown in Figure 15 using the previously discussed intensity threshold method. The time at which the boundary layer transitions from laminar to turbulent seems to vary slightly with Re_2 based on the experimental results shown in Figure 15b. In the time region immediately after t = 1 ms, the thickness profile corresponding to the highest Re_2 shows a rapid increase approximately 0.03 ms earlier than that of the lowest Re_2. There is little to no perceptible difference between the thicknesses across the test conditions within the laminar time region. The limited spatial resolution of the image data may be a contributing factor to this similarity. Additionally, the density gradients in the higher-Re_2 tests may be larger due to the increased initial density required to obtain the desired Reynolds number. The expected reduction in boundary layer thickness with higher-Re_2 experiments may be negated by the increased intensity gradients measured in these tests, which could cause the gradient threshold to be met at a further distance from the bottom wall. Since the boundary layer transition can be visualized even at x = 90 mm across all test conditions, then it is sure that the flow is turbulent at x = 103 mm where PCB 2 is installed by the time the reflected shockwave arrives there.

Based on the approximate transition time of 0.1 ms that was observed across the five test conditions, the critical Reynolds number Re_t was calculated by the following equation,

$$Re_t = \frac{\rho_2 u_2^2 t_{tr}}{\mu_2}, \tag{4}$$

where t_{tr} is the transition time based on the boundary layer profile. The resultant critical Reynolds numbers were found to vary between 100,000 and 200,000, depending on the test condition; further experiments using high-speed schlieren imaging and repeatability testing would greatly assist in realizing a more exact value for Re_t.

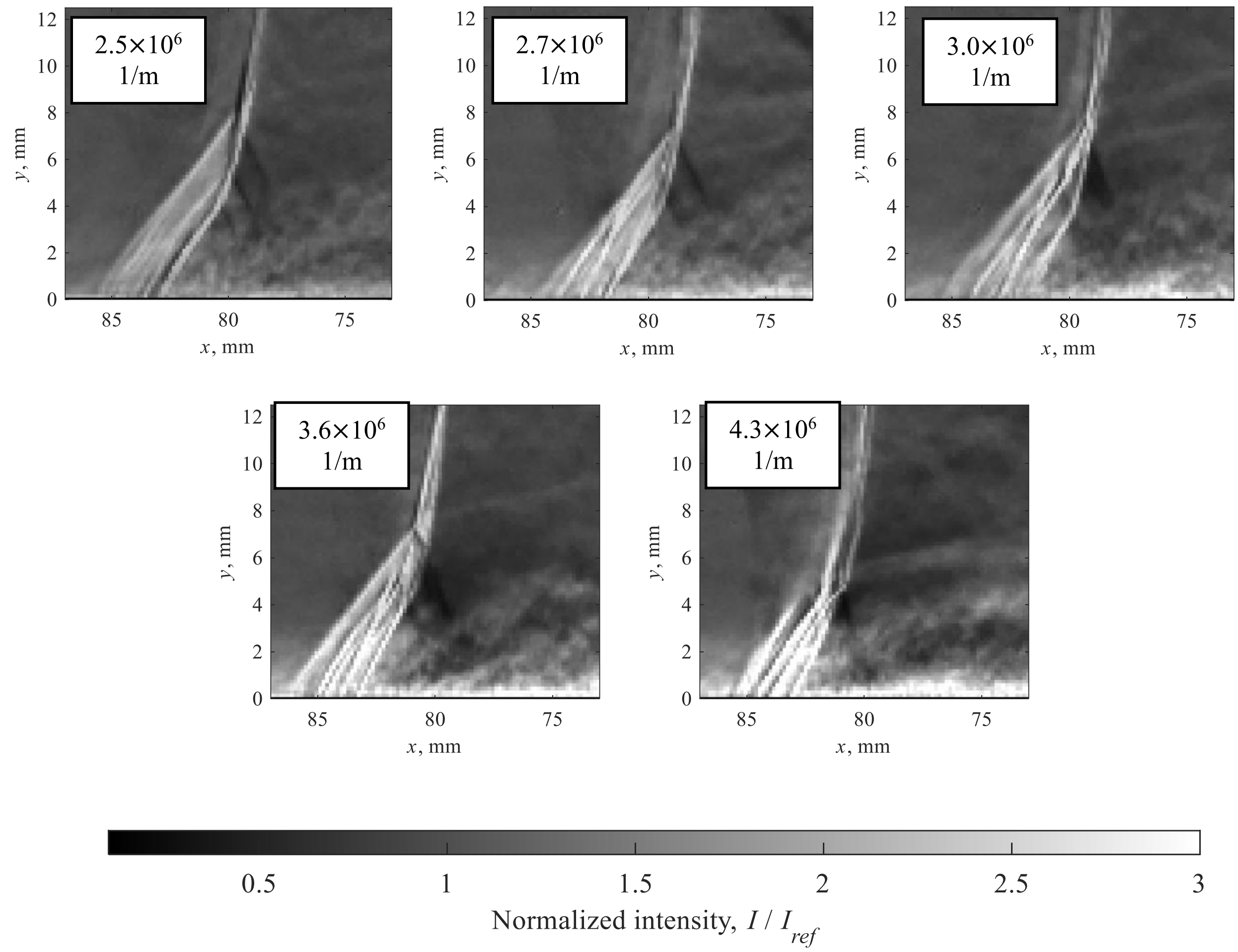

Figure 16. Shock bifurcation structure from all tests near *x* = 80 mm.

The condition of the bifurcation structure each time it arrives at $x = 80$ mm during each test can be seen in Figure 16. Regardless of the test condition, all of the shock bifurcations share some traits in common; the triangle-shaped foot shape is seen in all five of the images, as well as some bending of the normal shockwave above the bifurcation. Notably, the leading shock of each bifurcation appears to be succeeded by numerous additional shockwaves. This is a side-effect of the path-integrating nature of schlieren photography. If the streamwise location of the bifurcation foot's front edge varies in the spanwise axis (towards/away from the camera), any misalignment of the front edge will be visualized in the schlieren images.

Comparison of the bifurcations at the highest and lowest Re_2 in Figure 16 shows a difference in the height of the triple point at this distance from the endwall. The lowest Re_2 test, shown in Figure 16a, has the highest triple point with a height of 8 mm. The tests shown in Figure 16b-d share similar bifurcation heights near 7 mm, while the highest- Re_2 test, shown in Figure 16e, has a triple point height between 4 and 5 mm. The angle of the leading foot shock in all cases appears to be near 50° with respect to the bottom wall, which aligns with previous findings by Weber *et al.* and Matsuo *et al.* [18,33]. The contrast of the image appears to increase with Re_2, which aligns with the observations made in the boundary layer thickness discussion.

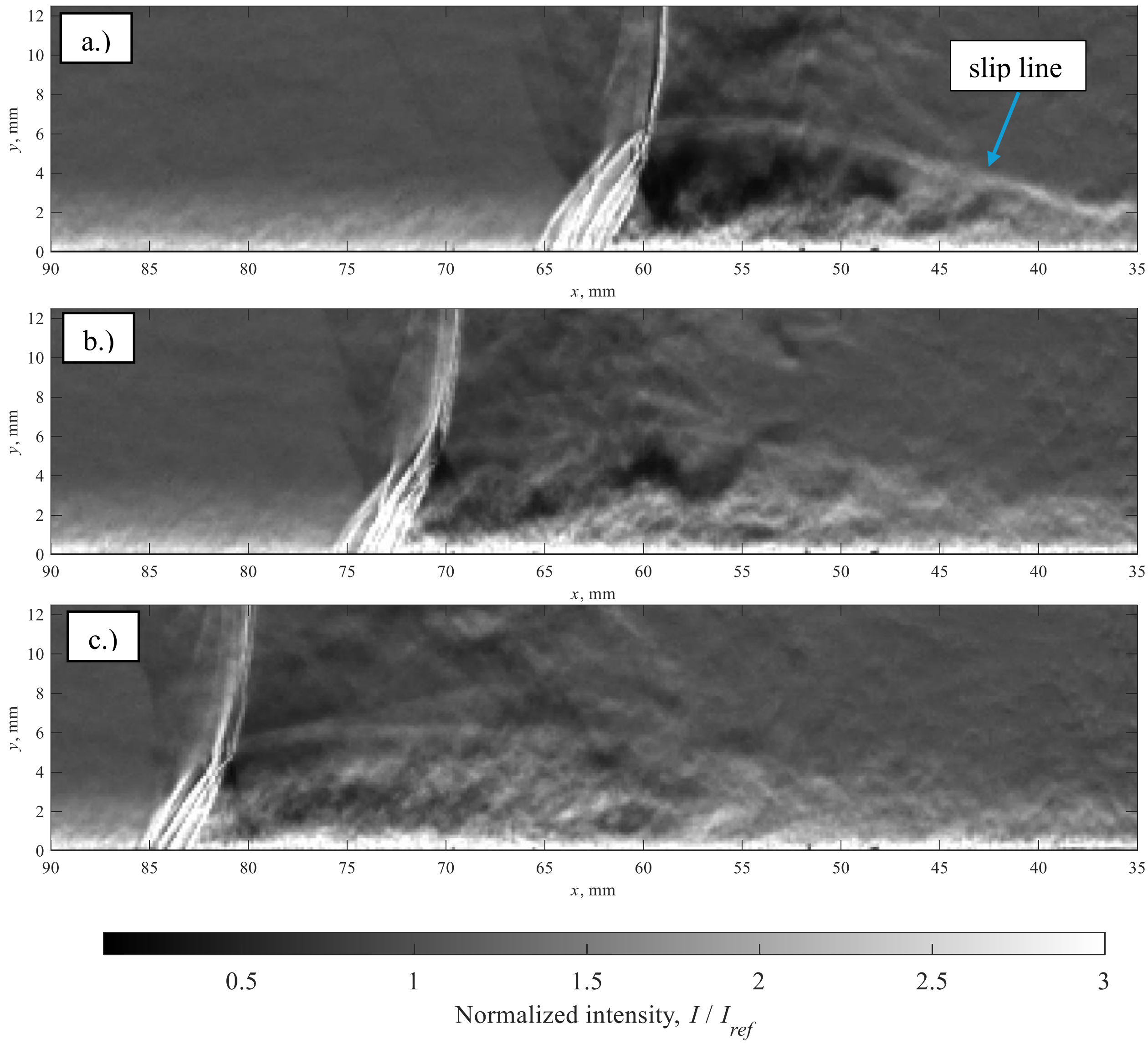

Figure 17. Dissolution of bifurcation bubble and slip line as the reflected shock wave travels through the visualization area. Re_2 = 4.3×10^6 1/m.

Figure 17 presents a clearer observation of the bifurcation bubble as it detaches from the rest of the structure and disperses. In Figure 17a, the bubble can be seen behind the bifurcation and stretches from x = 35 mm to x = 60 mm. The slip line, serving as the upper boundary of the bubble, is also present in this image. In Figure 17b, the slip line and the bubble are no longer clearly visible, though the slip line is weakly visible in Figure 17c. Also evident across the three images is a slight reduction in the height of the bifurcation; this is likely caused by the loss of the bifurcation bubble.

These phenomena do not appear to have a dependence on the test's Re_2, as the other tests show a similar reduction in bifurcation size and accompanying dissipation of the bubble near x = 70 mm.

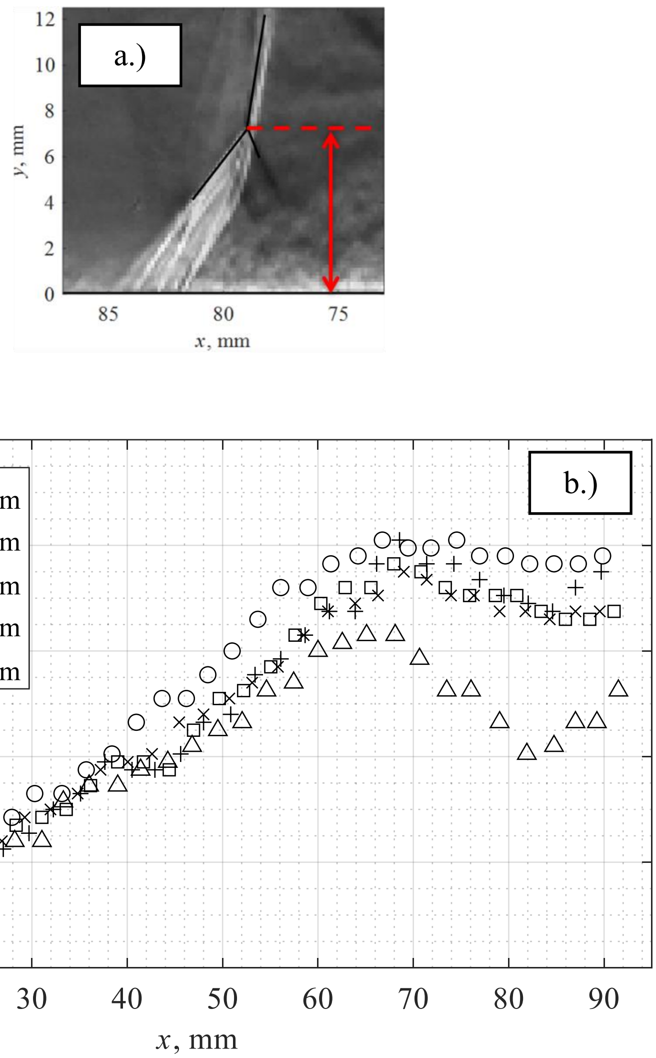

Figure 18. a.) Schematic showing the 'triple point' used to measure the bifurcation height relative to the sidewall. b.) Variations in bifurcation height as the reflected shockwave travels away from the endwall.

The data in Figure 18 was obtained by determining the location of the reflected shockwave bifurcation triple point along x and y in each frame of the high-speed schlieren data that was obtained. The lack of bifurcation height data for x < 10 mm is due to the inability to distinguish the bifurcation structure from the reflected shockwave or the bottom wall. Figure 18 shows that the bifurcation height increases linearly with respect to the distance between the shockwave and the endwall until it exceeds 60 mm. Extending the linear trend to $x = 0$ mm reflects a reduction in bifurcation height to almost 0 mm, which shows that the heights were correctly measured. For streamwise distances exceeding 60 mm, the bifurcation height reaches a maximum value before decreasing steadily. This trend is maintained across the range of Re_2 values that are shown, along with extremely similar bifurcation heights within this region. It is apparent that the bifurcation formed in the highest-Re_2 case experienced the most significant reduction in its height after $x = 60$ mm. It is unknown whether this was caused by the increased Reynolds number, as the large quantity of shock structures present in the images obfuscate the true triple point somewhat. It is certain, however, that the highest-Re_2 test case had the shortest bifurcation height in the post-60 mm range. The inclusion of repeatability tests would provide a clearer picture of the changes to the bifurcation height within each Reynolds number by reducing the impact of the variations in its structure, but this was not possible for this thesis.

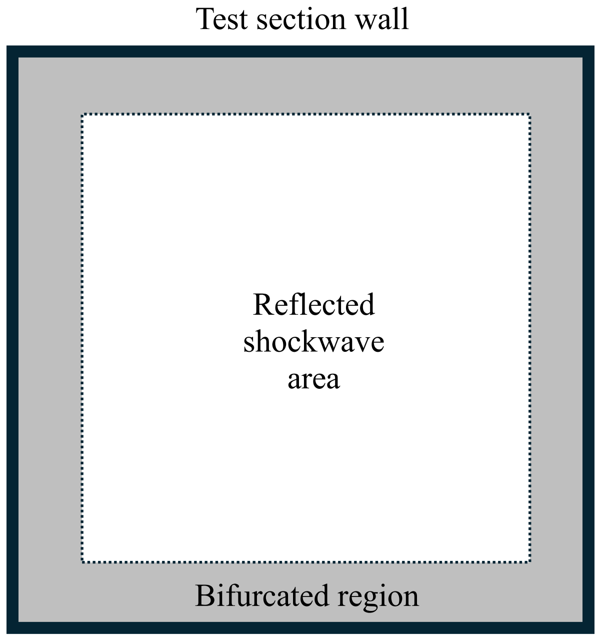

Figure 19. Schematic of penetration of reflected-shock bifurcation into the cross-sectional area of the test section for a bifurcation height of 8 mm

It is important to remark on the size of the reflected shock bifurcation relative to the internal area of the driven section. As seen in Figure 19, in the case of the lowest Reynolds number, the bifurcation height reaches a maximum value of 8 mm. A visual representation of the 8 mm-tall bifurcation size relative to the driven section's internal area is shown in Figure 19. If the bifurcation height is assumed to be 8 mm across its entire span at this moment, then the bifurcation itself is occupying approximately 40% of the driven section's cross-sectional area. This does not mean that 40% of the gas in region 2 is passing through the bifurcation instead of the normal component of the reflected shockwave, but it does present serious concerns regarding the contribution of the bifurcation to the nonideal effects present in the region 5 flow. The bifurcation has been shown to induce small-and-large scale vortices into the region 5 flow field along the walls; when the bifurcation structure is large, these vortices will also be large; similarly, when the bifurcation reaches further into the core flow of the driven section, the vortices generated by the bifurcation will further penetrate the core flow and contaminate the stagnant gas in region 5. It is for this reason that some shock tubes that focus on analysis of region 5 employ larger-diameter driven sections, which can greater preserve the core of the region 5 gas by decreasing the area affected by the bifurcation relative to the overall cross-section.

3.2. Pressure Data Analysis

After the 45 shock tube tests were completed, the voltage data recorded by the PCB sensors was imported into MATLAB and converted into units of pressure based on calibration constants provided by the manufacturer.

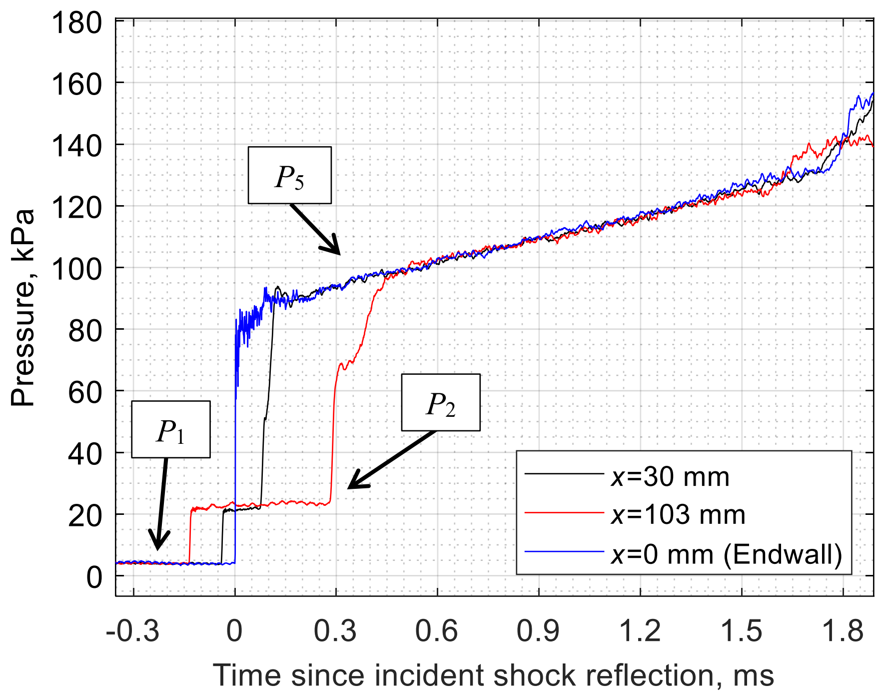

Figure 20. Typical pressure measurements within the test section before and after the reflection of the incident shockwave. Relevant pressure regions are noted.

Figure 20 shows the changes in pressure caused by the shock wave propagation through the shock tube and serves as a good representation of typical results from an individual shock tube test. This specific experiment was performed at Test Condition 6, with $M_s = 2.2$, $P_4 = 550$ kPa, and

P_1 = 4.2 kPa. At the beginning, all pressure signals indicate measurements near P_1. The furthest measurement from the end wall first experienced a rapid change in pressure to 22 kPa; soon thereafter, a similar pressure rise is seen in the measurement taken 30 mm from the endwall. Eventually, the measurement at the endwall indicated a large jump in pressure to approximately 80 kPa. This trio of events is the outcome of the incident shockwave passing through the driven section of the shock tube before eventually arriving at the endwall. Therefore, the measurement of 22 kPa reflects the value of P_2 in region 2, and 80 kPa reflects the initial value of P_5 in region 5.

The passage of the reflected shockwave through the driven section can also be visualized in the pressure recordings; additional step-like changes in pressure can be seen in the measurements taken 30 mm and 103 mm from the endwall. The total sequence of events is summarized as follows:

- The incident shockwave passes PCB2 at x = 103 mm.
- The incident shockwave passes PCB1 at x = 30 mm.
- The incident shockwave reflects off the endwall and is recorded by PCB3.
- The reflected shockwave passes PCB1.
- The reflected shockwave passes PCB2.

Even in this example, the non-ideal pressure fluctuations that were previously outlined can be seen in the pressure recordings. For example, the region 5 pressure increases over time rather than remaining constant. This is seen in all three of the pressure sensors. Pressure data recorded after t = 0.6 ms shows strong agreement between the three sensors, which ensures that the increasing trend is not caused by a measurement error. High-frequency pressure fluctuations can also be seen in this region across the three sensors.

The passage of the reflected shockwave over the sidewall pressure sensors is not accompanied by a single step-like change in pressure in this case. Instead, the pressure rise is halted prematurely before climbing rapidly to match that of the measurements by the endwall sensor. This is caused by the structure of the reflected shock bifurcation passing over the sensor rather than a single normal shockwave.

For the full analysis of the pressure measurements, measurements taken at a single sensor location will be shown across all of the test conditions performed at a specific shock Mach number. Due to the varying magnitudes of the pressure values themselves, the pressure data is normalized by dividing the pressure at each point by the initial driven gas pressure P_1. The pressure recordings themselves will be assessed first; more specific analysis topics such as growth rate and root-mean-square findings will be addressed later.

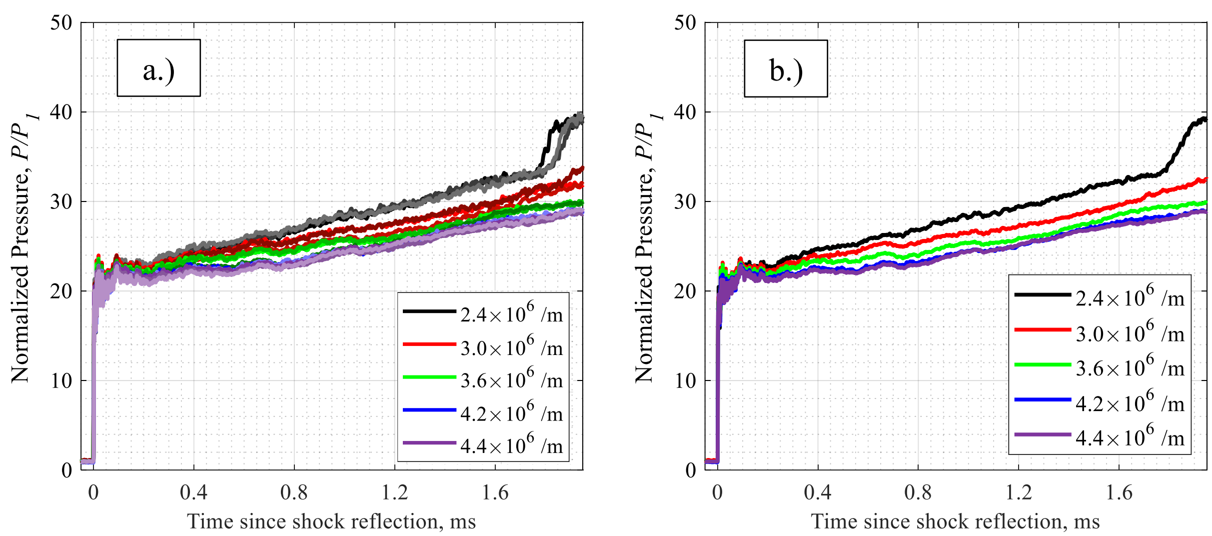

Figure 21. Pressure data recorded at the endwall a.) before and b.) after averaging each set of three experiments into a single curve. M_s = 2.2.

To simplify the presentation of the pressure data recorded at a specific Mach number, each set of three experiments performed at a specific test condition are averaged into a single curve. An example of this operation is shown in Figure 21. The averaging procedure is shown to not impact the overall depiction of large-scale fluctuations in the pressure data.

3.2.1 Pressure Data at M_s = 2.0

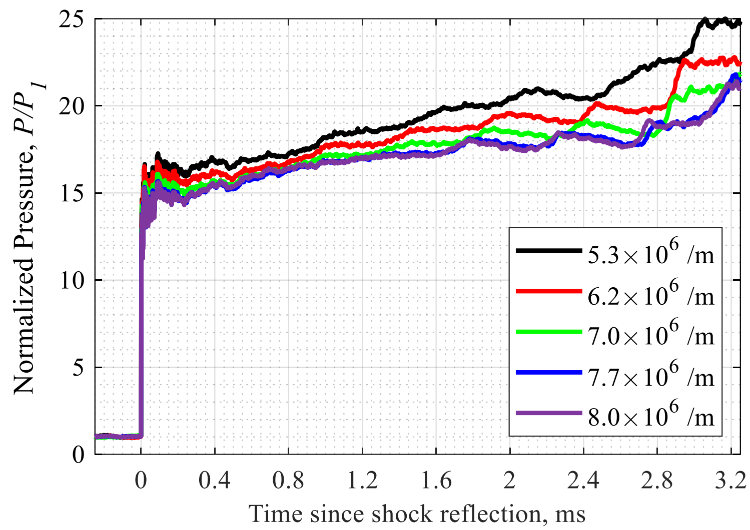

Figure 22. Pressure histories recorded at the endwall for Test Conditions 1-5 with M_s = 2.0.

The data in Figure 22 shows the rapid change from P_1 to P_5 after the reflection of the incident shockwave for M_s = 2.0. In this case, the time region corresponding to region 5 is from the moment of the shock reflection at t = 0 ms to the onset of further pressure growth near t = 2.5 ms. The pressure rise at the end of region 5 is caused by a pressure wave that originates from the interaction of the reflected shockwave with the contact surface. Several observations can be made from an initial inspection of the data. Initially, all of the test conditions produced similar pressures after the shock reflection. The expected region 5 pressure for this Mach number is P_5/P_1 = 15.0 based on one-dimensional shock theory; based on the data's initial P_5 measurements, the theoretical value was a close match to what was observed.

Shortly after the initial pressure rise is measured, the pressure begins to increase across the test conditions and continues until the end of region 5. While the pressure curves appear to match across the conditions for the first millisecond of post-reflection time, they begin to diverge while also exhibiting low-frequency fluctuations. By measuring the time between each peak in the fluctuations for a given test condition, their frequency can be determined; in this case, the waves repeat with a periodic interval of approximately 0.5 ms, which corresponds to a frequency of 2000 Hz. Previous experiments in the shock tube facility have shown that the tube exhibits a small amount of transverse and axial vibrations soon after the fast valve is opened that persist for much longer than the usable test time; this is likely caused by the reaction forces generated by rapidly releasing a large amount of gas from the driver section into the driven section. The vibrations appear to intensify as P_4 and P_1 are increased and are not believed to be caused by shock-induced phenomena. Attempts have been made to dampen the vibrations by increasing the weight of the hold-down fixtures used to keep the driven section stationary, but it has not been entirely mitigated. An additional detail to note is the small burst of high-frequency noise in the pressure data immediately after the shock reflection. This noise is believed to be caused by the impingement of the shock wave itself and not by a fluctuation in the flow ahead of the sensor face.

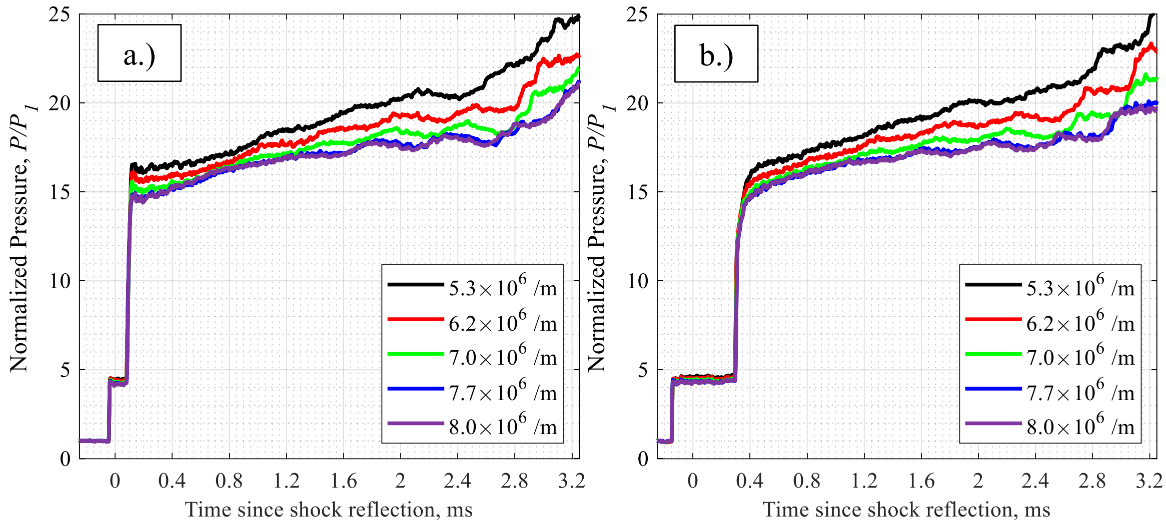

Figure 23. Measurement of pressure along the sidewall of the test section during the shock reflection. Data from Test Conditions 1-5 are shown. a.) PCB 1, *x* = 30 mm. b.) PCB 2, *x* = 103 mm.

The pressure along the top and bottom wall of the test section before and after the shock reflection can be seen in Figure 23. As expected, the sidewall measurements show the arrival of both the incident and reflected shockwave. These measurements have many features in common with the endwall measurements shown in Figure 22, including the gradual pressure growth and eventual onset of low-frequency waves. An interesting observation can be made regarding the trends in the pressure histories with higher Re_2 values in Figure 23a: the initial pressure growth in these curves is more severe but soon experiences a decrease in pressure. This is most evident in the curve corresponding to $Re_2 = 8.0\times10^6$ 1/m, where a reduction in the pressure growth occurs 0.7 ms after the shock reflection. Conversely, the curve corresponding to $Re_2 = 5.3\times10^6$ 1/m experiences a similar reduction at $t = 1.0$ ms, which is almost 40% later.

The measurements 103 mm from the endwall seen in Figure 23b do not indicate a significant variation in the pressure growth in the moments after the arrival of the reflected shockwave. Instead, the first millisecond of P_5 measurement (shown as $t = 0.4 - 1.4$ ms in the figure) shows remarkably similar pressure growth rates across the five test conditions. At this distance from the endwall, the boundary layer is turbulent at the time of the reflected-shock boundary-layer interaction; hence, it may be possible that the turbulent boundary layer can disrupt the typical influence of the shock bifurcation structure on sidewall pressure recordings, such as those by Sanderson [22].

3.2.2 Pressure Data at $M_s = 2.2$

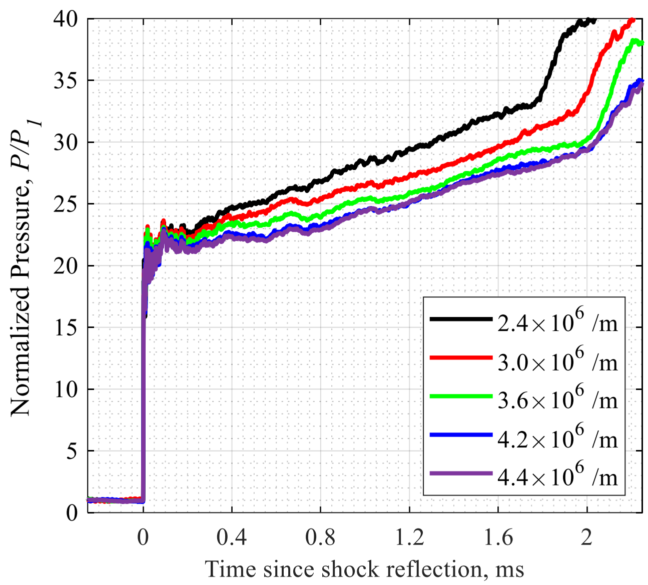

Figure 24. Test-averaged pressure histories recorded at the endwall for Test Conditions 6-10.

Test conditions 6-10 were conducted with a shock Mach number of 2.2 and a total change in Re_2 of two million per meter. It should be noted that the freestream Mach number in region 2 is supersonic for this set of data as well as for $M_s = 2.3$. While the implications of this on the pressure analysis are not entirely known, it is sure that disturbances in region 2 are only able to travel downstream for these two sets of experiments. The end wall pressure data seen in shows an increasing trend in the post-reflected shock pressure; in the right half of the figure, a prevalent jump in pressure occurs at slightly different times depending on the test condition's Re_2. The pressure jump for the lowest- Re_2 case occurs 1.75 ms after the shock reflection, while the highest-Re_2 case features the jump after 2 ms. Mirels theorized that the separation distance between the incident shock wave and the contact surface is proportional to P_2 and the square of the shock tube's diameter [34]. In the case that P_2 is reduced, the separation distance is reduced and the contact surface will be closer to the end wall by the time the reflected shock wave arrives. Since the lowest-Re_2 case shown in Figure 24 features the lowest P_2 value, then the shortened test time can be explained by the separation distance reduction proposed by Mirels.

Non-ideal pressure growth continues to impact the uniformity of the flow in region 5, though the low-frequency fluctuations observed at $M_s = 2.0$ are now absent. For this group of tests, the endwall pressure briefly matched the predicted value for P_5/P_1 of 20.4. Though all test conditions start with nearly the same initial value for P_5/P_1, they rapidly begin to diverge as time progresses.

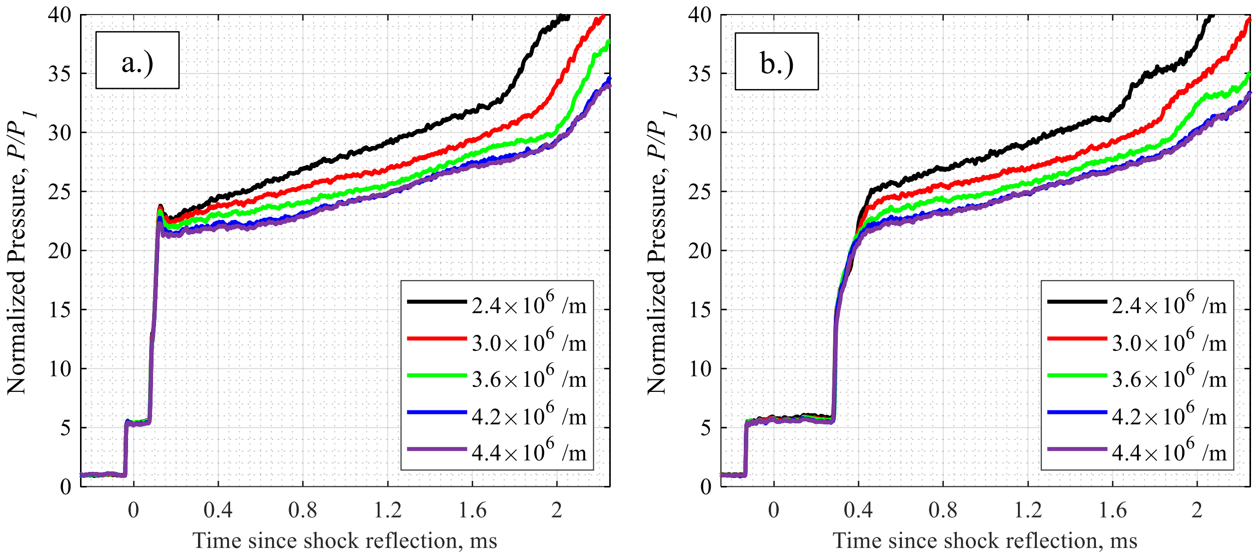

Figure 25. Test-averaged measurements of pressure along the sidewall of the test section during the shock reflection. Data from Test Conditions 6-10 are shown. a.) PCB 1, *x* = 30 mm. b.) PCB 2, *x* = 103 mm.

The pressure recordings along the sidewall for Test Conditions 6-10 are shown in Figure 25. The pressure history immediately after the passage of the reflected shockwave varies between the two measurement locations. In Figure 25a, at approximately 0.1 ms, the post-reflected shock pressure reaches a maximum value before diminishing and returning to a generally increasing state. This matches Sanderson's predictions of a small pressure bump mentioned previously [22]. However, this trend does not appear to persist further from the endwall, as the curves Figure 25b do not feature this overshoot. Sanderson mentioned that the pressure overshoot is based on the assumptions of steady laminar flow through the reflected-shock boundary-layer interaction. At this distance from the endwall, the boundary layer is turbulent, which disrupts the bifurcation structure and reduces the likelihood of a clear stagnation streamline existing downstream of the interaction. Despite the lack of a pressure overshoot in Figure 25b, the pressure curves exhibit a reduction in slope once the normalized pressure approaches 15. Once the normalized pressure reaches that of the mean flow, the slope decreases again to match that seen in Figure 25a until the end of region 5 is reached. This matches the trend seen in the data captured by PCB 2 for Test Conditions 1-5, which further points to the possibility of the turbulent boundary layer causing changes to the pressure variations experienced behind the bifurcated shockwave.

3.2.3 Pressure Data at M_s = 2.3

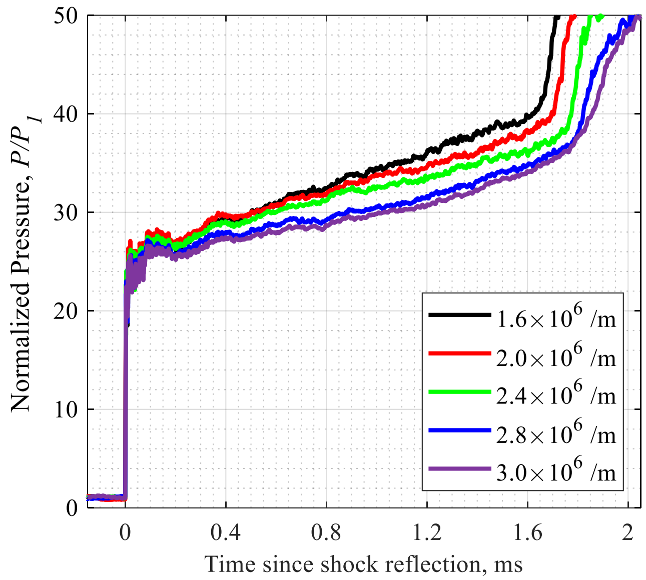

Figure 26. Test-averaged pressure histories recorded at the endwall for Test Conditions 11-15.

The final set of test conditions were designed to achieve M_s = 2.3, the highest in this study. These experiments also featured the lowest range of freestream Reynolds numbers due to the low initial pressures required to increase P_4/P_1. The resulting pressure measurements at the endwall, seen in Figure 26, show remarkable similarities to those in Figure 24, though the usable region 5 test time has been reduced to a minimum of 1.6 ms. For this Mach number, the expected value for P_4/P_1 is 23.5; in reality, this value was only maintained for an extremely short period before the pressure began to rise.

The data captured at the lowest Re_2 continues to reflect the greatest level of pressure growth within region 5, though this is less clear during the first millisecond of test time. A noticeable bump in the pressure data occurs at t = 0.4 ms across all of the test conditions at this Mach number; the pressure curves begin to diverge soon after its arrival. Prior to the bump, all pressure curves maintain similar trends and do not diverge. The divergence of the pressure curves appears to continue until approximately t = 1.2 ms, when the data for Re_2 = 2.8 and 3.0 $\times 10^6$ 1/m show a small, but noticeable increase in growth over time. These two test conditions also show the most significant divergence after the bump at t = 0.4 ms. The exact source of this bump is not known.

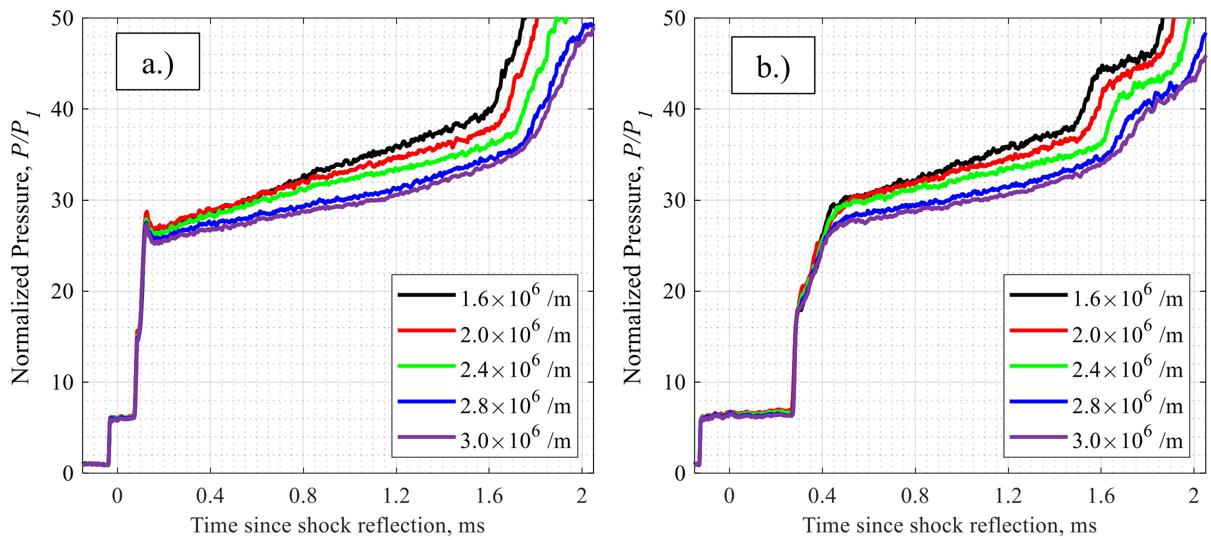

Figure 27. Test-averaged measurements of pressure along the sidewall of the test section during the shock reflection. Data from Test Conditions 11-15 are shown. a.) PCB 1, x = 30 mm. b.) PCB 2, x = 103 mm.

The pressure recordings taken at M_s = 2.3 along the sidewalls of the shock tube can be seen in Figure 27. The pressure overshoot seen by PCB 1 is slightly greater than in the experiments at M_s = 2.2, but the pressure measurements are visually similar to the previous set of data. The pressure rise near t = 1.6 ms is much stronger in this set of results; this is likely caused by a stronger transmitted pressure wave from the interaction of the reflected shockwave with the contact surface. The bump observed at t = 0.4 ms at the endwall in Figure 26 is not seen in either of the sidewall measurements. However, the pressure divergence at 0.4 ms can be seen in the sidewall measurements at $x = 30$ mm. The data recorded at $x = 103$ mm does not show a pressure overshoot after the passage of the reflected shockwave.

3.2.4 Preliminary Observations

For all test conditions, it was seen that the experimental data for P_5/P_1 initially matched their predicted values from one-dimensional shock tube theory. Soon after region 5 was established, the data indicated a gradual increase in pressure that varied depending on the Reynolds number. The tests at higher Mach numbers suffered shorter test times but lacked the low-frequency waves seen at $M_s = 2.0$. Based on these observations, it was clear that a more quantitative approach would be necessary to characterize the pressure fluctuations and identify any potential causes of their presence.

3.3 Analysis of Non-Ideal Pressure Fluctuations

3.3.1 Anomalies in Sidewall Pressure Measurements Behind the Reflected Shockwave

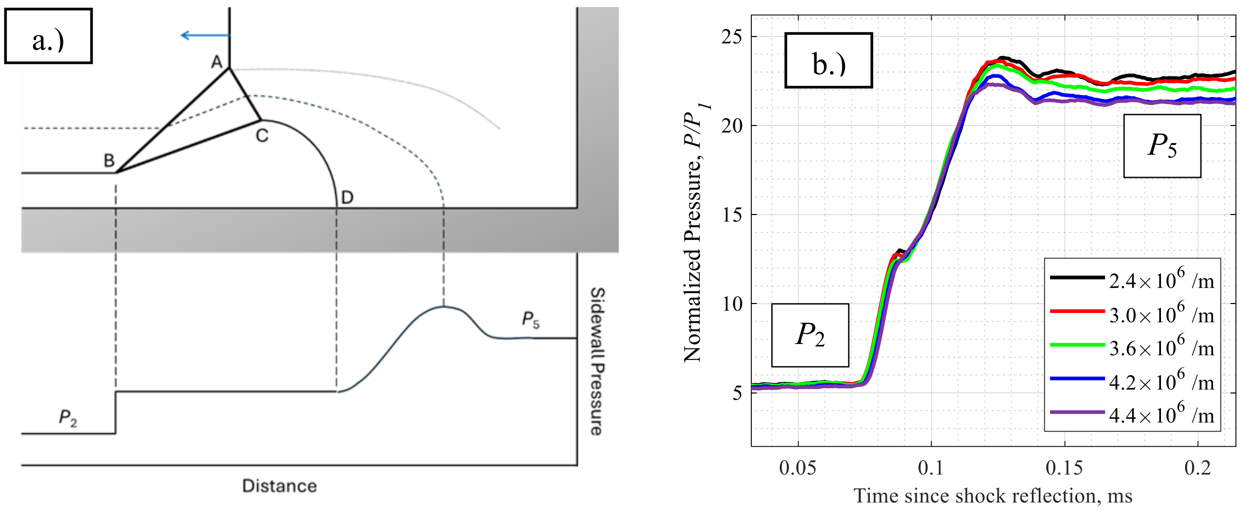

Figure 28. Comparison between predicted (a) and observed (b) pressure fluctuations as observed along the sidewall behind the reflected shockwave for PCB 1. Test conditions 6-10.

It was noticed that measurements of the pressure behind the reflected shockwave by PCB 1 and PCB 2 indicated non-steplike changes in pressure from P_2 to P_5. In the case of PCB 1—shown in Figure 28—the region 2 pressure rapidly increases near 0.08 ms before prematurely stabilizing for a brief period of time near 0.09 ms. This is quickly followed by a second rapid increase in pressure that subsequently decreases to approach the pressure values that were observed at the endwall at this point in time. When the predicted and observed pressure fluctuations are compared side-by-side, clear parallels can be drawn between the two. It is reasonable to assume based on these similarities that the pressure overshoot is caused by the presence of a stagnation streamline within the recirculation region behind the bifurcated shockwave. The schlieren data corroborates the fact that the boundary layer was laminar at the time that the shockwave-boundary layer interaction was passing over PCB 1, which would further indicate that the predicted conditions were being reproduced as indicated by the sensor.

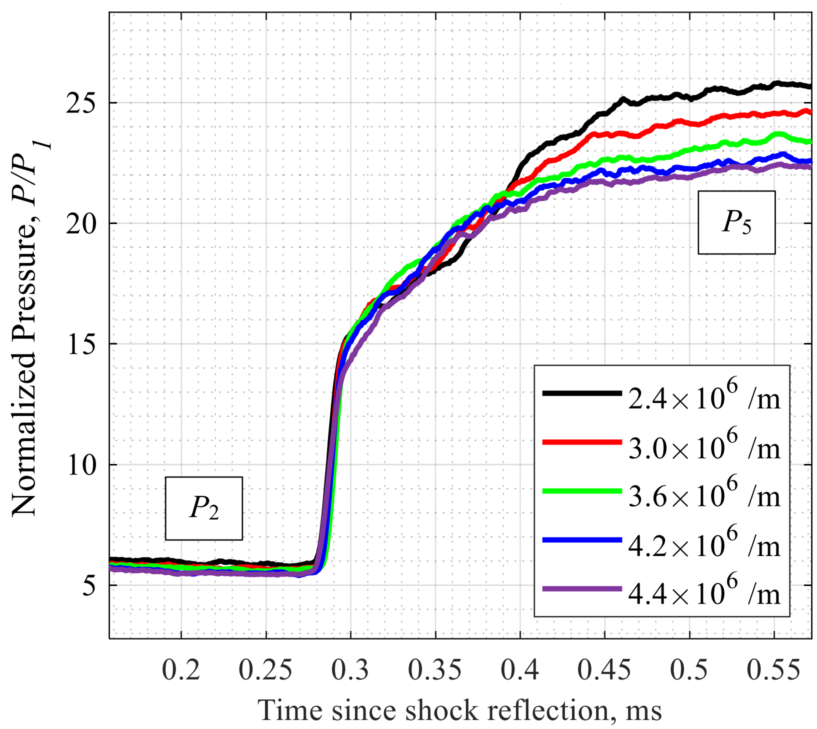

Figure 29. Close-up view of the change in pressure from P_2 to P_5 as measured by PCB 2 at x = 103 mm from the endwall. Test conditions 6-10.

For the measurements taken by PCB 2, a few of the non-steplike pressure fluctuations can still be observed as the bifurcated shockwave passes over the sensor. Specifically, rather than rapidly jump from P_2 to P_5, the pressure prematurely ceases to rapidly grow and instead steadily increases from an intermediate value to P_5 before stabilizing. However, the brief cessation of pressure change between P_2 and P_5 is no longer present, and the pressure overshoot is either too minimal to observe or is absent altogether. Based on the high-speed schlieren data, a turbulent boundary layer is present at the streamwise location where PCB 2 is located by the time the bifurcated shockwave arrives there. It is possible that the turbulent boundary layer disturbs the streamlines that are otherwise predictable, and may therefore prevent a stagnation streamline from forming and impinging on the sidewalls of the driven section. Future work on this topic should consider locating a PCB sensor within the high-speed schlieren visualization area while also positioned such that the boundary layer is turbulent when the bifurcated shockwave arrives; for this experimental setup, such a location could be any streamwise distance between x = 60 mm and x = 95 mm from the endwall.

3.3.2 Pressure and Temperature Growth

A quantitative analysis of the pressure growth in region 5 was desired. Previous studies have standardized the measurement of growth rate by determining the nondimensional change in pressure over a specific period of time using a linear curve-fit; the time span may range from the first millisecond of test time or the timespan encompassing the region 5 test duration. In either case, the linear fit is used to determine what percent change in pressure would be experienced over the course of a single millisecond. This is shown as

$$\frac{dP^*}{dt} = \frac{\frac{P - P_i}{P_i}}{\Delta t} \tag{5}$$

where P^* represents the relative change in pressure, P_i represents the initial pressure within the timespan, and Δt represents the span of time between P and P_i. dP^*/dt is typically multiplied by 100 to show the pressure change as a percentage, so the unit of dP^*/dt is shown as percentage divided by the time elapsed.

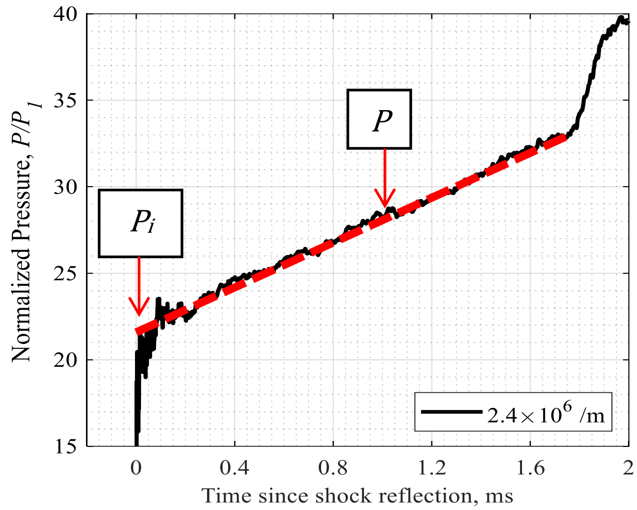

Figure 30. Demonstration of pressure growth rate calculation based on pressure measurement at the endwall. Test condition 6, M_s = 2.2.

To provide a single value for the pressure growth over an entire flow region, a linear curve fit is found for the pressure data within the region. The curve fit is then used to estimate the initial pressure (i.e. the initial value of the linear curve within the time region) as well as the pressure at a time 1 ms after the initial value. These values are then used in the dP^*/dt equation shown above, and the unit of the result is %/ms to reflect the change in pressure after a single millisecond. A visual representation of this procedure is shown in Figure 30 for reference.

It was originally theorized that the non-ideal pressure growth in region 5 is primarily influenced by a non-uniform pressure distribution in region 2. Therefore, the pressure growth in region 2 will also be assessed. As PCB 2 is furthest from the endwall, it experiences the largest duration of region 2 flow compared to region 1, so the region 2 pressure recordings by PCB 2 will be investigated.

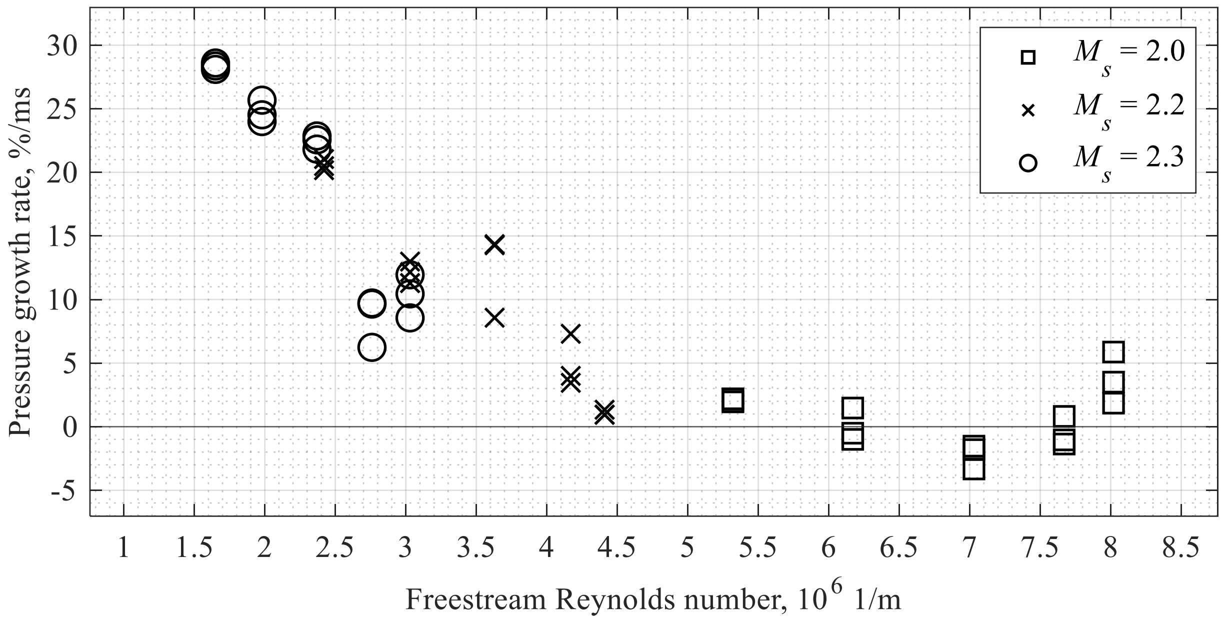

Figure 31. Influence of freestream Reynolds number on the non-ideal pressure growth in region 2, based on measurements by PCB 2 at x = 103 mm.

The growth rate in P_2 was determined through the linear curve-fit technique for each experiment and is shown in Figure 31 based on their respective freestream Reynolds numbers. At lower Reynolds numbers, such as those obtained at M_s = 2.3, the pressure growth is substantial, with experiments at the lowest Re_2 producing growth rates in P_2 of up to 28 %/ms. As Re_2 increases, the intensity of the pressure growth begins to weaken. For $Re_2 = 2.4 \times 10^6$ 1/m, the P_2 growth had diminished to roughly 22 %/ms. Crucially, this Reynolds number was achieved for M_s values of 2.2 and 2.3; the growth rates from both sets of experimental data at this Reynolds numbers reflect similar values, though for M_s = 2.3 the growth rate was slightly higher. The data for the aforementioned Mach numbers features an additional overlap at $Re_2 = 3 \times 10^6$ 1/m, and the growth rates again reflect similar amounts between the two cases, though this time the data at M_s = 2.2 indicates the higher growth rate. For freestream Reynolds numbers at or greater than 4.4×10^6 1/m, the observed growth rate in P_2 is quite small. In some cases, the growth rate is even negative, indicating a higher P_2 near the incident shockwave than near the contact surface. In general, the pressure growth rate in region 2 appears to decrease as the freestream Reynolds number increases, though some outliers to this hypothesis exist (especially at the higher Reynolds numbers).

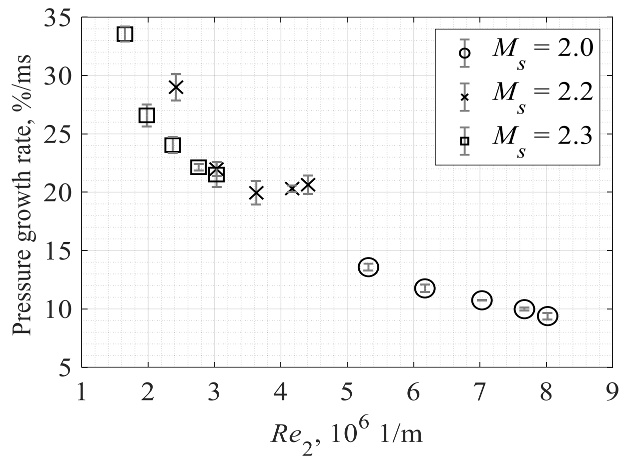

Figure 32. Influence of freestream Reynolds number on the non-ideal pressure growth in region 5 measured at the endwall.

The growth rate in P_5 for each test was found and shown in Figure 32. The entirety of region 5 was used for determining the linear curve fit of each set of pressure data. Many of the trends observed in Figure 31 can also be seen here, including the overall reduction in growth rate as the Reynolds number is increased. The tests with noticeable pressure growth in region 2 experienced significant amounts of growth in region 5. Across the entire range of Re_2, the pressure growth in region 5 appears to be greater than it was in region 2.

Within M_s = 2.3, the growth rate in region 5 was reduced from 33 %/ms to 22 %/ms by increasing the freestream Reynolds number. This indicates that Re_2 can indeed be successfully used to reduce the growth of P_5 without requiring a change in M_s. For M_s 2.2, the growth of P_5 decreased from 29 %/ms to 20 %/ms, though the change occurred predominantly in the lower- Re_2 range. The higher- Re_2 range for this M_s did not exhibit any significant changes in the pressure growth. The pressure growth values recorded for M_s = 2.0 are the lowest of the entire set of experiments, with an average growth rate of 11 %/ms. The decreasing trend with respect to Re_2

remains valid for this Mach number, but the amount of pressure growth lost by increasing Re_2 is less significant within this range.

As an additional note, the temperature is also known to increase over time in region 5. The normalized temperature growth rate $\mathrm{d}T^*/\mathrm{d}t$ follows a similar format to its pressure-based counterpart:

$$\frac{dT^*}{dt} = \frac{\frac{T - T_i}{T_i}}{\Delta t}. \tag{6}$$

However, Petersen and Hanson found that $\mathrm{d}T^*/\mathrm{d}t$ can be determined with $\mathrm{d}P^*/\mathrm{d}t$ through isentropic relations by

$$\frac{dT^*}{dt} = \frac{dP^*}{dt}\left(\frac{\gamma - 1}{\gamma}\right)\left(\frac{P}{P_i}\right)^{\gamma-1} \tag{7}$$

and uses similar units of (%/ms) [12].

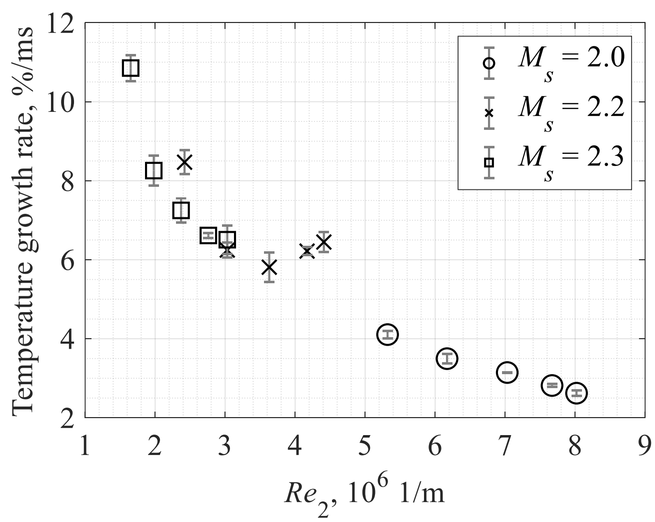

Figure 33. Estimation of temperature growth in region 5 based on pressure measurements.

Using Eqn. 5, the temperature growth after the shock reflection was estimated for each of the tests based on the measurements of dP_5^*/dt and is shown in Figure 33. As expected, the tests with the largest amount of pressure growth experienced the same with respect to temperature. The tests at $Re_2 = 1.6 \times 10^6$ 1/m experienced temperature growth of more than 10 %/ms, the most severe of the entire set of experiments. The least severe temperature growth of 2.5 %/ms occurred at the highest Reynolds number.

3.3.3 Temporal Analysis of Growth Rate

As seen in Figure 27a, the pressure growth in region 5 does not appear to linearly increase for some test conditions. To measure the changes in pressure growth over the entire span of region 5, an additional analysis technique was developed. The function of this technique is as follows.

Instead of analyzing the entirety of region 5 all at once, a "window" of a user-specified width is defined that is smaller than the total size of region 5. Starting at the beginning of region 5 flow, a linear fit is applied to the pressure data within the window. The growth rate is calculated based on the linear fit and is recorded at the point in time corresponding to the middle-most data point within the window. The window is marched forward in time by one step, i.e. 1 μs, and the process is repeated until the window reaches the end of region 5. The window behavior is similar to what is seen in a moving-average filter, but the calculation performed within the window is different in this case.

The result of this process is a smooth curve that indicates the local growth rate in the pressure data at each moment in time within region 5. The definition of local growth rate must be specified; this process only takes changes in P_5 *within the moving window* into account, rather than changes with respect to the initial value of P_5.

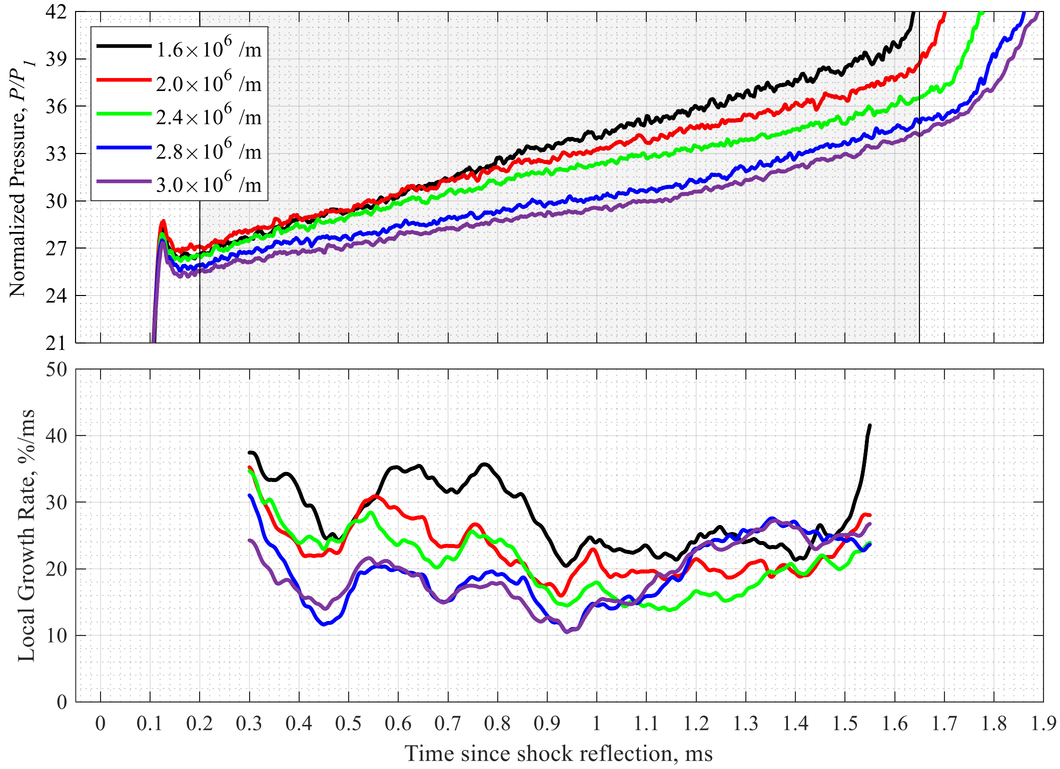

Figure 34. Changes in pressure growth rate over time shown alongside the original pressure data recorded at M_s = 2.3 by PCB 1. Growth rates were found within a 201-point moving window.

The fluctuation of dP_5^*/dt over the duration of the test time can be seen in Figure 34. During the first half of the test time, the experiments performed at lower freestream Reynolds numbers immediately exhibit an increased amount of pressure growth than the others. This is especially apparent between 0.4 ms to 1 ms; during this time, the most significant differences in pressure growth across the five test conditions can be seen. The duration of region 5 after this point features more uniform growth rates across the range of experiments, with most conditions featuring a growth rate between 20-25 %/ms at the end of the test time.

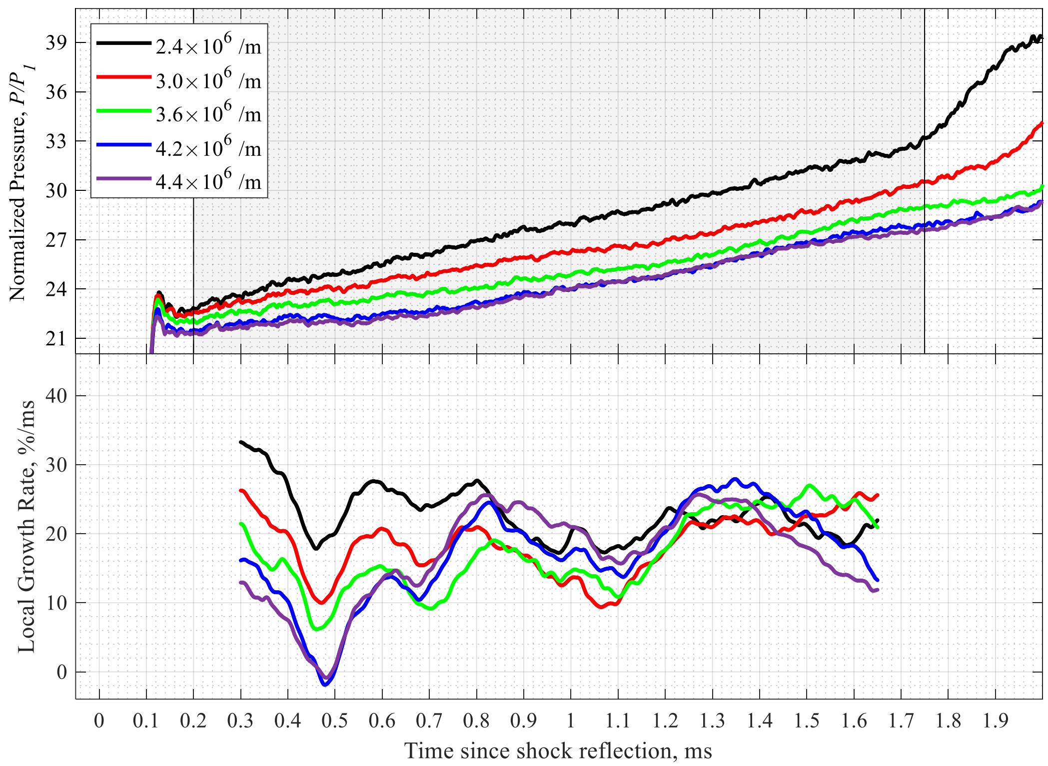

Figure 35. Changes in pressure growth rate over time shown alongside the original pressure data recorded at M_s = 2.2 by PCB 1. Growth rates were found within a 201-point moving window.

The local growth rate fluctuations for M_s = 2.2 can be seen in Figure 35. Like the results for M_s = 2.3, the growth rates are most varied during the first half of the test time for region 5, with a consistent spread of almost 20 %/ms between the tests corresponding to the highest and lowest Reynolds numbers from the beginning of region 5 until approximately 0.5 ms. At this moment, the growth in P_5 is halted temporarily in the higher-Re_2 tests before beginning to increase again shortly afterwards. After 0.8 ms, the growth rates across the five experiments become less dispersed; by 1.2 ms, the local growth rates are close to the same value across the range of tests.

The data for Re_2 = 4.2 and 4.4 × 10^6 1/m indicate the most substantial fluctuations in pressure growth across the total test time, with changes in growth rate of more than 25 %/ms across the first half of region 5. In contrast, the data at $Re_2 = 2.4 \times 10^6$ 1/m only indicate a change in growth rate of 15 %/ms. Though the low-Re_2 test may have a higher growth rate on average, it remains much more consistent and predictable throughout the test time; in some situations, this may be preferable due to increased predictability of P_5 over time.

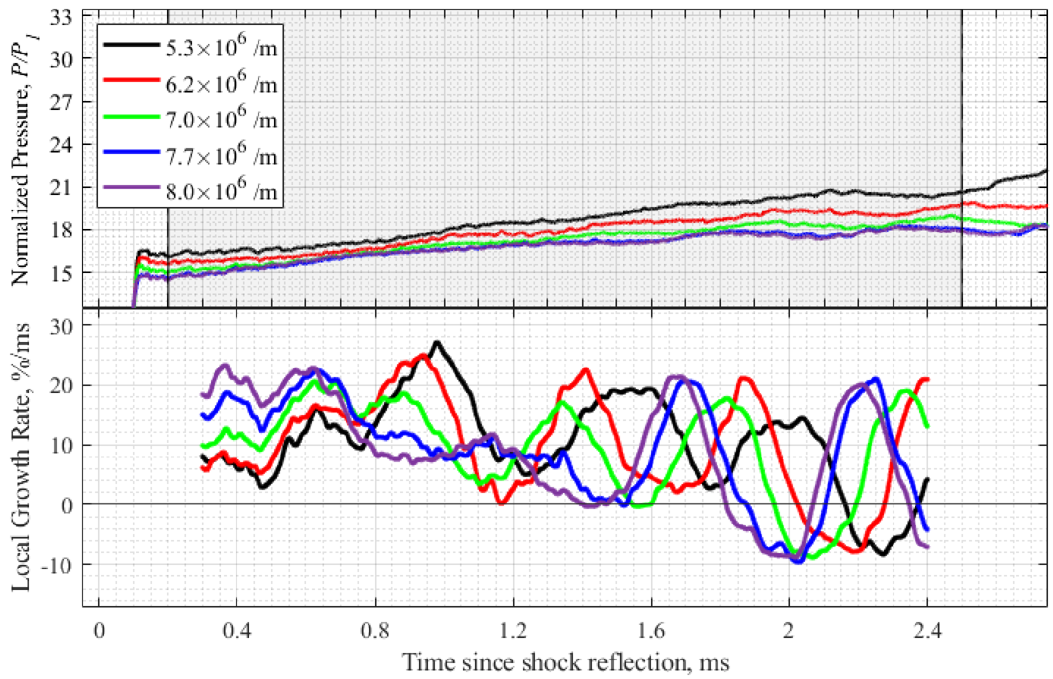

Figure 36. Changes in pressure growth rate over time shown alongside the original pressure data at $M_s = 2.0$ by PCB 1. Growth rates were found within a 201-point moving window.

For the case of $M_s = 2.0$, the time-variant trends in dP_5^*/dt shown in Figure 36 are the most difficult to interpret due to the low-frequency waves that are present.The growth rates at the beginning of region 5 show a different pattern than what was observed for the higher-M_s experiments: the higher-Re_2 tests initially experienced more significant pressure growth than their lower-Re_2 counterparts. At about $t = 0.8$ ms, this trend is reversed, and after $t = 1$ ms the pressure waves obfuscate the true trends in pressure growth for the duration of the test time. At some points in the latter half of region 5, the growth rates for all five of the test conditions dropped below 0 %/ms for short periods of time.

3.3.3.1 Growth Rate Discussion

The overall decreasing trends in growth rate with respect to Re_2 are in line with theoretical expectations. If the boundary layer thickness is inversely proportional to the freestream Reynolds number, then low-Reynolds number flows will generate thicker boundary layers, which, according to Mirels, result in more substantial nonuniformities in the gas within region 2 [8]. This explains the elevated growth rates seen in the experiments at lower Reynolds numbers in Figure 31. Furthermore, the elevated growth rates at lower Reynolds numbers in region 5 follow theoretical expectations set by Rudinger, who claimed that nonuniformities present in region 2 would be transmitted into region 5. Curiously, though the higher- Re_2 tests indicated minimal or even negative growth rates in P_2, growth rates greater than 10 %/ms were still observed in P_5. This implies that control of the non-homogeneity of the gas in region 2 is not sufficient to totally remove the growth of P_5.

By showing the time-varying changes to the non-ideal pressure growth in region 5, numerous observations can be made that would not otherwise be possible. For example, the time period where Re_2 appears to make the most significant impact on the growth rate is in the first few fractions of a millisecond after the passage of the reflected shockwave. During this time, the lower-Re_2 experiments experienced the highest (but most stable) pressure growth, while those at higher Re_2 values had lower pressure growth, but more significant fluctuations overall. Notably, these trends were only valid for M_s = 2.2 and 2.3, while for M_s = 2.0 the opposite trends were observed. Despite this initial change in the growth rate trend, the overall growth rates for M_s = 2.0 seen in

Figure 32 reflect that the higher-Re_2 tests still yielded the lowest average amounts of pressure growth.

The implications of these results have the most value for experiments requiring minimal variation in P_5, such as chemical combustion and ignition delay analysis. For these types of experiments, if Re_2 is to be adjusted, two choices are available:

a.) Use a lower freestream Reynolds number, which provides a more stable—but higher—pressure growth over the course of region 5, or

b.) Use a higher freestream Reynolds number, which results in lower—but more erratic—pressure growth.

Either way, the freestream Reynolds number has now been shown to serve as a potential means of modifying the pressure growth rate without requiring significant changes to the experimental setup. Based on the results in Figure 32, increasing the freestream Reynolds number generally results in less pressure growth in region 5, with an increased effectiveness at higher shock Mach numbers.

3.4 Frequency and Root-Mean-Square Analysis

With the large-scale changes in P_5 now addressed, the effect of Re_2 on the more small-scale changes in P_5 is next to be assessed. A general view of the frequency spectra obtained from the pressure signals can help identify any frequencies that are of interest or are from other sources than the flow itself.

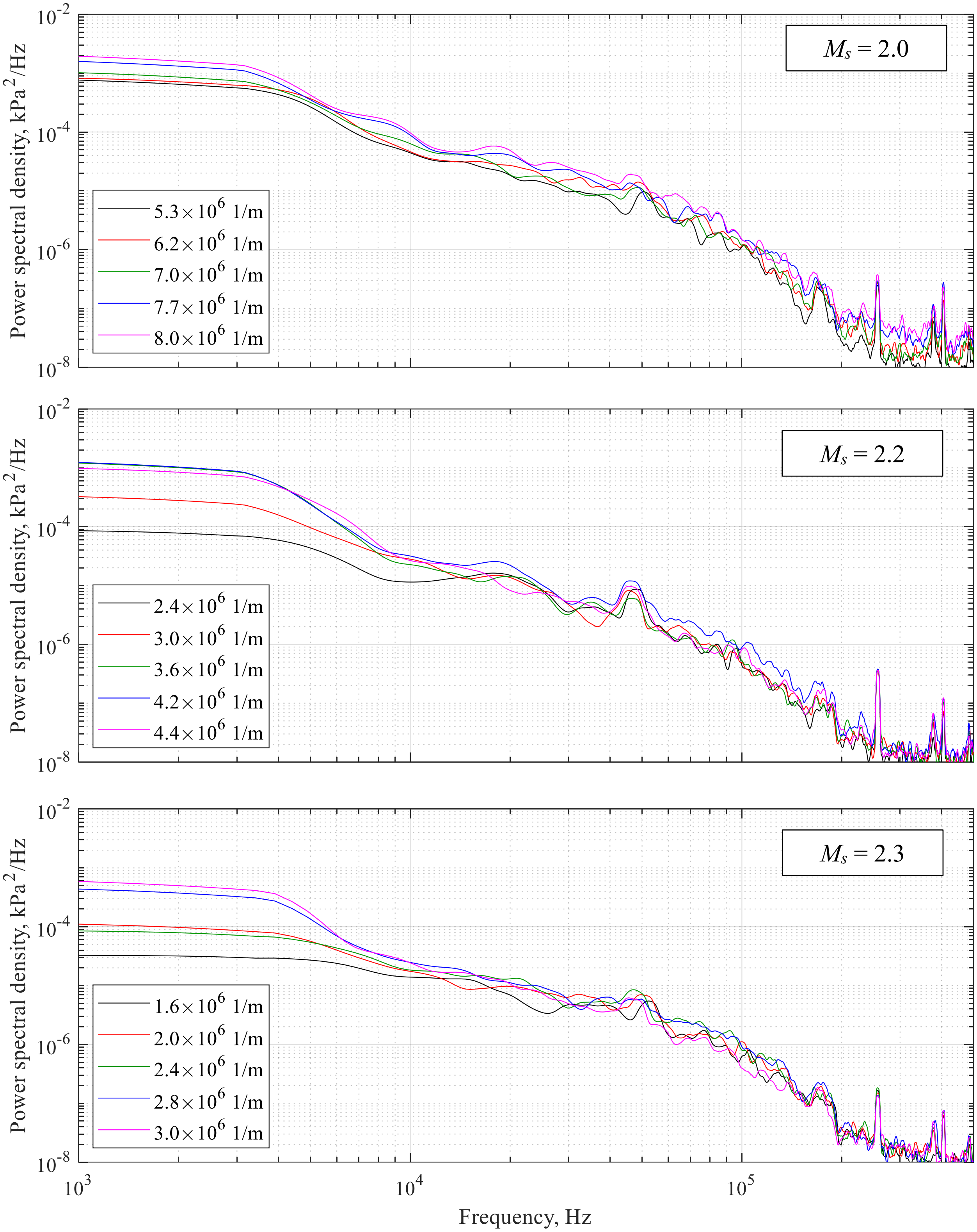

Figure 37. Power spectral densities of the pressure in region 5 measured at the endwall across a range of freestream Reynolds numbers and Mach numbers.

The power spectral density curves shown in Figure 37 reflect a consistent frequency spectrum across the tests that were performed. Welch's method was used to calculate the PSDs shown, with a window size of one-eighth of the total number of samples per test and 50% overlap between windows [35]. To improve the quality of the PSDs, the three sets of pressure data acquired at a given Re_2 were concatenated to yield a single measurement of P_5 with triple the length. The PSDs indicate that the spectral power of frequencies below 10kHz is quite high; this frequency range includes the frequencies at which the shock tube itself vibrates during an experiment. Also apparent is a series of high-frequency spikes at 250 kHz and 400 kHz; these frequencies also appear in PSDs taken before the test begins, so they are presumed to be caused by electrical noise and not by flow phenomena.

With a preliminary assessment of the pressure signals' frequency spectra complete, the root-mean-square (RMS) of the pressure fluctuations in each experiment will be examined. Traditionally, to calculate the RMS value for a signal, the signal must be centered along a specific axis such that its mean amplitude is close or equal to zero. The application of this technique to the pressure signals presents two problems that should be adequately addressed. First, the average pressure in region 5 is much greater than zero with an overall-increasing trend caused by the non-ideal pressure growth discussed previously. Second, the pressure signals are shown to experience both high-frequency (greater than 10 kHz) and low-frequency (less than 10 kHz) fluctuations. Even if the pressure growth is negated via a linear detrend, both of these fluctuation types will persist in the data and impact calculation of RMS.

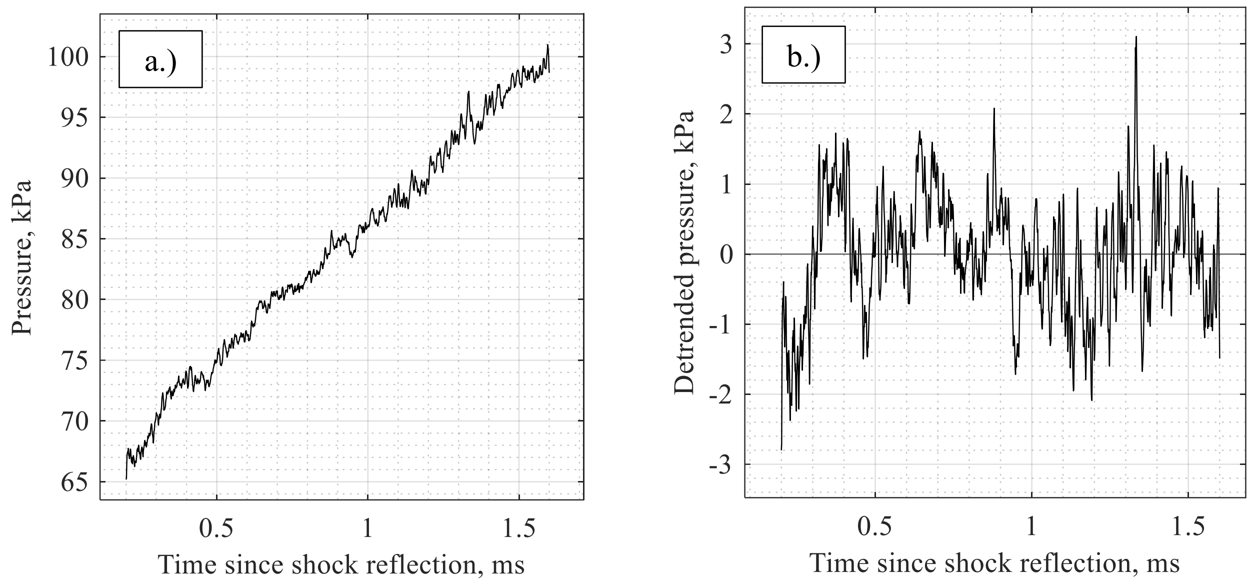

Figure 38. Effectiveness of pressure signal preparation for RMS calculations by subtracting a linear curve-fit. Data shown is from Test Condition 11 and recorded at the endwall. a.) Original pressure signal. b.) Pressure signal after the subtraction.

Solutions to these two problems will now be outlined. To overcome both the non-zero average pressure in region 5 and the non-ideal pressure growth, a linear curve-fit is found for the pressure data; by subtracting the linear curve-fit from the pressure data, the average pressure of the overall signal is much closer to zero. An example of the implementation of this method is shown in Figure 38. While the pressure growth has been successfully removed from the pressure data, some low-frequency waves present in Figure 38b will continue to negatively influence calculations of RMS.

For this study, the higher-frequency fluctuations in P_5 will be focused on due to the importance of the freestream noise in the shock tube in hypersonic shock tunnel research. Furthermore, interpretation of the low-frequency fluctuations would be complicated by the physical oscillations of the shock tube facility that may obfuscate fluid phenomena-induced fluctuations within this frequency range. Therefore, the low-frequency oscillations should be removed from the pressure data to narrow the investigation to the intensity of the higher-frequency fluctuations. This achieved through an application of MATLAB's highpass filter to the pressure data after the linear curve-fit has been subtracted from it. The low-frequency limit for the filter was chosen to be 10 kHz to remove the shock tube oscillations and other facility-dependent effects.

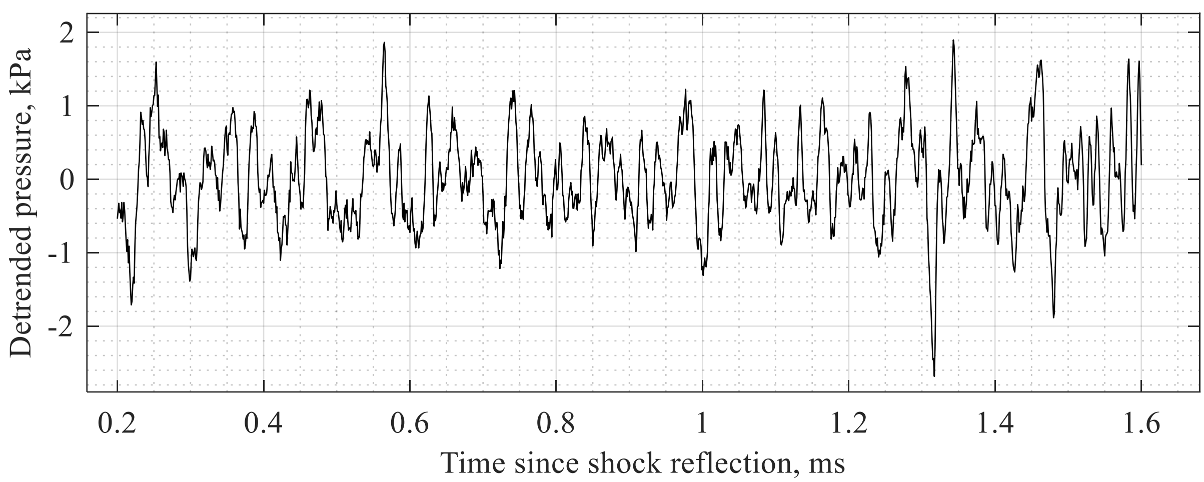

Figure 39. Application of high-pass filter to pressure data to remove low-frequency oscillations. Pressure data is from Test Condition 11 and recorded at the endwall.

The disappearance of broad changes of P_5 in Figure 39 shows that the high-pass filter effectively reduces the low-frequency pressure fluctuations that were still present in Figure 39. A high-pass filter with a lower limit of 10 kHz was applied to the pressure data. The actual determination of the RMS values in region 5 was subsequently performed for each individual test to observe any impact of Re_2 on the pressure fluctuations. The measurements taken by the PCB sensor at the endwall were used for this portion of the RMS analysis due to its direct measurement of region 5 without experiencing the effects of the reflected shockwave bifurcation.

Like the growth rate analysis, a start and end time was chosen for each Mach number to define the span of region 5 flow. In this case, the start time for all tests was chosen to be 0.2 ms after the shock reflection. Though a slightly earlier start time could be chosen, this would then include the shock-induced vibration of the PCB sensor in the RMS calculation. Such a vibration is not present in the flow itself, and it would dramatically increase the perceived RMS measurement. The upper time limit on region 5 varies depending on the shock Mach number. For tests with M_s = 2.0, the upper limit is 2.5 ms; for those at M_s = 2.2, the upper limit is reduced to 1.7 ms; at M_s = 2.3, the upper limit is further reduced to 1.6 ms.

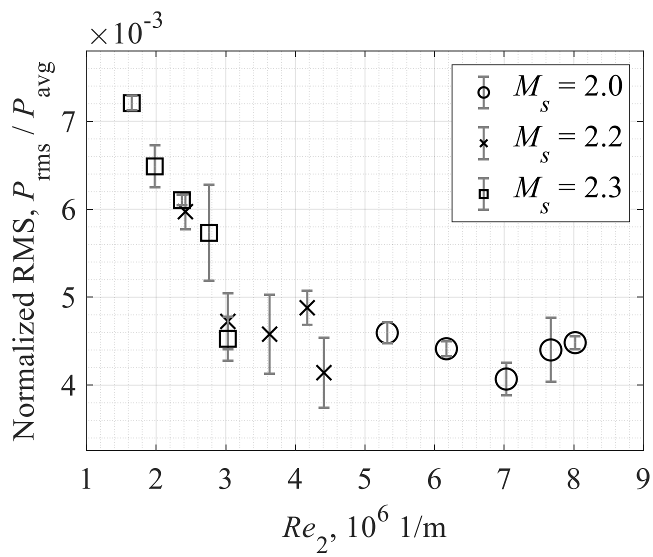

Figure 40. Effect of Re_2 on high-frequency pressure fluctuations measured in region 5 at the endwall.

The root-mean-square pressure measurements in regino 5 were calculated by

$$\frac{P_{\text{rms}}}{P_{\text{avg}}} = \frac{1}{P_{\text{avg}}}\sqrt{\frac{1}{n}\sum_{i=1}^{n}(P_i)^2}$$

where fluctuations in the detrended, filtered pressure signal P_i were evaluated. The average value for P_5 was used to normalize the RMS value for each experiment. This was repeated for each of the three experiments performed at a given test condition; the average normalized RMS value is shown for each test condition in Figure 40, while the error bars represent the standard deviation of the mean based on the distribution of the results found for each experiment.

Figure 40 reflects some similar trends to those seen in the dP^*/dt data shown previously. Notably, for the data within M_s = 2.2 and 2.3, a strong decreasing trend can be seen in the RMS data as Re_2 increases. At the lowest Re_2 near 1.6×10^6 1/m, the normalized RMS was near 0.007; with Re_2 near 4.5×10^6 1/m, this value dropped significantly to values near 0.004. Furthermore, the decreasing trend seems to be continuous between these two sets of results, though some spread is seen between the individual results at some Re_2 values. The implication of this finding is that, for lower freestream Reynolds numbers, the intensity of pressure fluctuations in region 5 are more significant compared to the mean pressure in the same region. Conversely, the higher- Re_2 tests (still relating to M_s = 2.2 and 2.3) experienced less intense pressure fluctuations in the region 5 flow. This implies that higher-Re_2 tests may be more desirable for shock tube applications that necessitate quieter flow in region 5, especially if the magnitude of P_5 is not so important (in these experiments, the lower- Re_2 experiments also had lower P_5 values overall).

For the data obtained at M_s = 2.0, the decreasing trend is no longer present in the RMS data. From what can be observed, the normalized RMS values do not show a dependence on the freestream Reynolds number and instead remain slightly above 0.004 across the investigated range of Re_2. Despite the lack of a decreasing trend at this Mach number, the normalized RMS values found are still among the lowest across the entire range of freestream Reynolds numbers and Mach numbers tested in this study. It is difficult to state for certain if this range of Reynolds numbers would still result in the lowest RMS values in the case that the shock Mach number was increased. For example, if freestream Reynolds numbers of 5 to 8×10^6 1/m were achievable with a shock Mach number of 2.2, higher RMS values may occur than with M_s = 2.0. Execution of this experimental procedure in other shock tube facilities with wider ranges of available Reynolds numbers may help determine the consistency of pressure fluctuation trends seen within this range of Re_2 values.

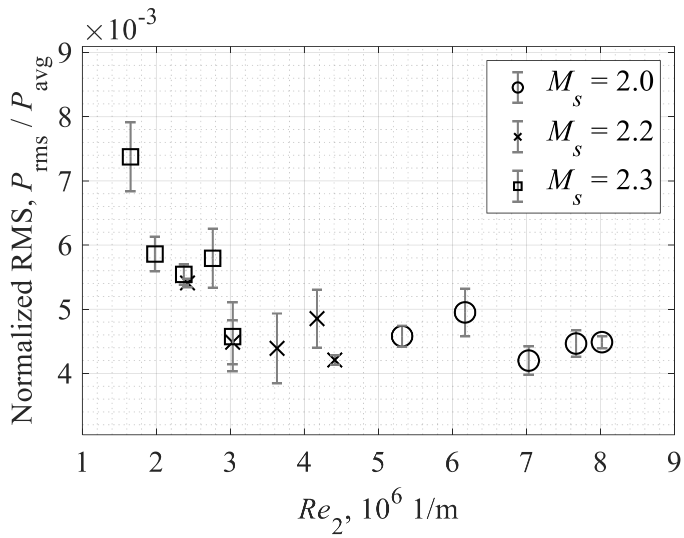

Figure 41. Effect of Re_2 on high-frequency pressure fluctuations measured in region 5 along the sidewall at x = 30 mm (PCB 1).

The pressure fluctuation intensity measured by the sidewall PCB sensors was also of interest in this study. In reflected-type shock tunnels, there is no way to measure the magnitude of pressure fluctuations at the surface of the diaphragm, so sidewall measurements remain as one of the only ways to assess the quality of the gas in region 5. Figure 41 shows the normalized RMS values of the pressure fluctuations in region 5 as measured by PCB 1. At the highest shock Mach number, the decreasing trend between normalized RMS and Re_2 has been preserved, and the lowest- Re_2 experiment continues to indicate the highest RMS value across the test campaign. For M_s = 2.2, the decreasing trend is significantly weaker, while for M_s = 2.0 there is no perceivable trend across the Re_2 range. On average, tests at M_s = 2.3 have the highest normalized RMS pressure levels, while tests at M_s = 2.2 and 2.0 reflect lower RMS levels. The pressure measurements taken along the sidewall also indicate lower normalized RMS values overall compared to those at the endwall seen in Figure 40. The larger spread in RMS results at this location decrease the applicability of a curve fit, so one has not been applied to the data in this case.

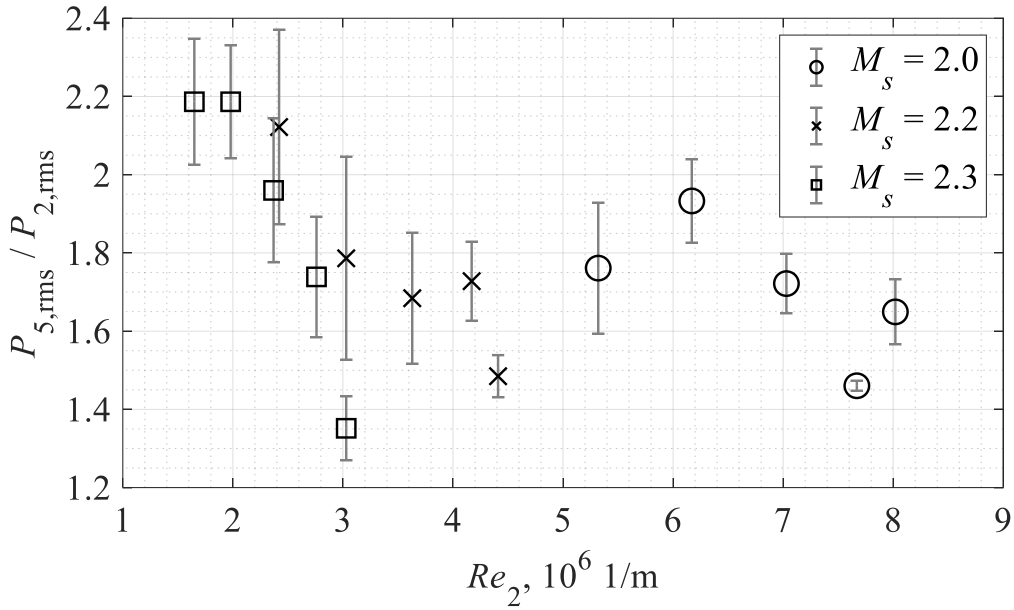

Figure 42. Amplification of pressure fluctuation intensity across the reflected shockwave by PCB 2 at x = 103 mm.

Previous studies by Trolier and Duffy have investigated the amplification of freestream turbulence in the air before and after the reflected shock wave [24]. Their work revolved around use of the hot-wire anemometer and their measurements focused on fluctuations in temperature and density of the test gas. By defining an amplification ratio based on the ratio of RMS values for density or temperature before and after the reflected shockwave, they were able to show that the RMS measurements were amplified differently depending on the freestream Reynolds number. The results shown in Figure 42 seek to emulate the analysis strategy used by Trolier and Duffy, but with RMS pressure measurements serving as the focal point. The RMS measurements of high-frequency pressure fluctuations in P_5 were divided by the accompanying RMS values for P_2 and plotted against the freestream Reynolds number. Due to the need to have an adequate length of region 2 flow to calculate RMS, only results from PCB 2 can be evaluated.

There is a noticeable level of error in the data shown in Figure 42, so overall trends in the data are obfuscated. For data with M_s = 2.3, an overall decrease in the amplification ratio is observed as the freestream Reynolds number increases. For M_s = 2.2, the decreasing trend is severely reduced, with the middle-to-high- Re_2 results showing a stagnation in the trend for this shock Mach number as the amplification ratio stabilizes near 1.5 after $Re_2 = 3.0 \times 10^6$ 1/m. For M_s = 2.0, the amplification ratio increases and decreases between different parts of its respective Re_2 range, with an average amplification ratio near 2.0. Of the test conditions evaluated, the data at $Re_2 = 4.5 \times 10^6$ 1/m shows the lowest average RMS amplification ratio across the reflected shockwave, while the data at $Re_2 = 2 \times 10^6$ 1/m shows the highest RMS amplification ratio.

3.4.1 Discussion

The trends seen in the RMS data largely mirror those found in the pressure growth data; lower RMS levels are observed in experiments performed at higher freestream Reynolds numbers. In this case, however, the reductions in RMS appear to taper off after $Re_2 = 3.0 \times 10^6$ 1/m. The RMS amplification ratio also approaches a minimum value at this freestream Reynolds number. For these reasons, it is proposed that shock tube experiments could be planned to operate with Re_2 values greater than three million per meter to help minimize the intensity of high-frequency pressure fluctuations in the test section after the reflected shockwave travels through the driven section. If the freestream Reynolds number is increased past this point, there may be minimal or nonexistent additional reductions to the RMS intensity, though the pressure growth over time may be further minimized in doing so.

Chapter 4: Concluding Remarks

4.1 Conclusion

The freestream Reynolds number has been shown to significantly influence the significance of the shock bifurcation caused by the shockwave-boundary layer interaction seen in shock tube experiments; furthermore, it has been shown that increasing the freestream Reynolds number can reduce the size of the bifurcation and lessen the strength of the non-ideal pressure fluctuations seen in pressure measurements taken in region 5. To properly observe the flow behind the reflected shockwave, a new test section was designed and manufactured in-house before being installed onto the High-Speed Aerothermodynamics Laboratory's shock tube facility and utilized for experiments. High-speed schlieren photography and pointwise pressure measurements were used to develop an understanding of the flow structures and fluctuations present in the test section during the experiments. Tests performed at higher Reynolds numbers had reduced pressure growth and decreased fluctuation intensity, both of which are desirable for those performing research with the gas in region 5. The most significant variations with respect to Reynolds number were observed at the beginning of region 5; by the end of region 5, the trends were more consistent across the test conditions. The size of the bifurcation foot formed on the reflected shockwave was also reduced by increasing the Reynolds number.

With these findings, it has been shown that modulation of the freestream Reynolds number may be a valid method for improvement of the test conditions produced by shock tubes in research endeavors that involve them. If reflected-type shock tunnel operators increase Re_2 in the shock tube portion of their setup, then the level of nonuniformity in their reservoir gas should be reduced significantly, which can in turn produce high-speed flows that maintain a more uniform condition throughout an experiment. Similarly, those using shock tubes for the study of chemical kinetics should increase the freestream Reynolds number if they are encountering an untenable level of pressure and temperature growth in region 5. Other techniques, such as modification of the test gas species or inclusion of different inserts into the driver section, may also be implemented to further improve the quality of the gas in region 5, of course. The value of these findings lie in the simplicity of their implementation into future experiments; there is no significant added cost associated with changing the freestream Reynolds number, and no permanent modifications to the experimental setup is required. In this regard, increasing the freestream Reynolds number can be seen as less of a significant inclusion into a testing procedure, and more of a simple—yet effective—means of producing higher-quality results with no added cost or complication into the procedure.

4.2 Future Outlook

There are two primary means of increasing the scope of this work while improving the quality of the findings. The range of evaluated test conditions could be greatly expanded, both regarding the freestream Reynolds number and the shock Mach number. As of the time of writing, there is no available method to modify the initial temperature of the driven gas; if some form of temperature control is added to the driven section, the viscosity of the test gas could be adjusted which would allow additional control over the Reynolds number. If the maximum operating pressures of the shock tube were increased, a larger range of initial pressures could be reached which would add additional range to the available Reynolds numbers.

This study only focused on three discrete shock Mach numbers: 2.0, 2.2, and 2.3. If the general guidelines of this experiment—vary Re_2 while keeping M_s constant—were followed at new M_s values, the validity of the findings could be assessed across a wider range of Mach numbers. For example, data recorded at $M_s = 2.1$ is sorely missing from this thesis. Inclusion of data at this Mach number would provide results at overlapping Reynolds numbers to those achieved within $M_s = 2.0$ and 2.2. Mach numbers less than 2 and greater than 2.3 would also be a valuable inclusion. If air is used as both the driver and driven gases, it is difficult to obtain Mach numbers greater than 2.3 without requiring unreasonably high pressure ratios; therefore, future work may require using driver gases like helium to increase the upper limit of shock Mach numbers that are evaluated.

Direct analysis of temperature fluctuations in region 5—specifically, along the sidewalls and near the rear corners—would also provide valuable insights into the homogeneity of the flow. Previous research has shown that bifurcation allows a cold jet of gas to travel along the walls of the shock tube. Temperature distributions along the sidewalls of the shock tube in this region have been investigated previously, such as by Ozawa using temperature-sensitive paints [36]. However, such an effort has not been made to evaluate the temperature distribution on the endwall. It is possible that the vortex formed by the cold-gas jet in the rear corner could be detected through temperature measurements on the endwall or near the corner.

References

[1] Glass, I. I., and Patterson, G. N., "A Theoretical and Experimental Study of Shock-Tube Flows," *Journal of the Aeronautical Sciences*, Vol. 22, No. 2, 1955, pp. 73–100. https://doi.org/10.2514/8.3282

[2] Sod, G. A., "A Survey of Several Finite Difference Methods for Systems of Nonlinear Hyperbolic Conservation Laws," *Journal of Computational Physics*, Vol. 27, No. 1, 1978, pp. 1–31. https://doi.org/10.1016/0021-9991(78)90023-2

[3] Belford, R. L., and Strehlow, R. A., "Shock Tube Technique in Chemical Kinetics," *Annual Review of Physical Chemistry*, Vol. 20, No. 1, 1969, pp. 247–272. https://doi.org/10.1146/annurev.pc.20.100169.001335

[4] Persico, G., Gaetani, P., and Guardone, A., "Dynamic Calibration of Fast-Response Probes in Low-Pressure Shock Tubes," *Measurement Science and Technology*, Vol. 16, No. 9, 2005, p. 1751. https://doi.org/10.1088/0957-0233/16/9/006

[5] Andreotti, R., Colombo, M., Guardone, A., Martinelli, P., Riganti, G., and di Prisco, M., "Performance of a Shock Tube Facility for Impact Response of Structures," *International Journal of Non-Linear Mechanics*, Vol. 72, 2015, pp. 53–66. https://doi.org/10.1016/j.ijnonlinmec.2015.02.010

[6] Liu, Y., and Kendall, M. A. F., "Numerical Analysis of Gas and Micro-Particle Interactions in a Hand-Held Shock-Tube Device," *Biomedical Microdevices*, Vol. 8, No. 4, 2006, pp. 341–351. https://doi.org/10.1007/s10544-006-9596-z

[7] Sutherland, W., "LII. *The Viscosity of Gases and Molecular Force*," *The London, Edinburgh, and Dublin Philosophical Magazine and Journal of Science*, Vol. 36, No. 223, 1893, pp. 507–531. https://doi.org/10.1080/14786449308620508

[8] Mirels, H., "Attenuation in a Shock Tube Due to Unsteady-Boundary-Layer Action," Jan 01 1957.

[9] Mirels, H., "Laminar Boundary Layer behind Shock Advancing into Stationary Fluid," Mar 01 1955.

[10] Mirels, H., "Boundary Layer behind Shock or Thin Expansion Wave Moving into Stationary Fluid," May 01 1956.

[11] Rudinger, G., "Effect of Boundary-Layer Growth in a Shock Tube on Shock Reflection from a Closed End," *The Physics of Fluids*, Vol. 4, No. 12, 1961, pp. 1463–1473. https://doi.org/10.1063/1.1706244

[12] Petersen, E. L., and Hanson, R. K., "Nonideal Effects behind Reflected Shock Waves in a High-Pressure Shock Tube," *Shock Waves*, Vol. 10, No. 6, 2001, pp. 405–420. https://doi.org/10.1007/PL00004051

[13] Hargis, J. W., and Petersen, E. L., "Shock-Tube Boundary-Layer Effects on Reflected-Shock Conditions with and Without CO2," *AIAA Journal*, Vol. 55, No. 3, 2017, pp. 902–912. https://doi.org/10.2514/1.J055253

[14] Nativel, D., Cooper, S. P., Lipkowicz, T., Fikri, M., Petersen, E. L., and Schulz, C., "Impact of Shock-Tube Facility-Dependent Effects on Incident- and Reflected-Shock Conditions over a Wide Range of Pressures and Mach Numbers," *Combustion and Flame*, Vol. 217, 2020, pp. 200–211. https://doi.org/10.1016/j.combustflame.2020.03.023

[15] Mark, H., "The Interaction of a Reflected Shock Wave with the Boundary Layer in a Shock Tube," NACA-TM-1418, March 1958.

[16] Petersen, E. L., and Hanson, R. K., "Measurement of Reflected-Shock Bifurcation Over a Wide Range of Gas Composition and Pressure," *Shock Waves*, Vol. 15, No. 5, 2006, pp. 333–340. https://doi.org/10.1007/s00193-006-0032-3

[17] Davies, L., and Wilson, J. L., "Influence of Reflected Shock and Boundary-Layer Interaction on Shock-Tube Flows," *The Physics of Fluids*, Vol. 12, No. 5, 1969, p. I-37-I–43. https://doi.org/10.1063/1.1692625

[18] Matsuo, K., Kawagoe, S., and Kage, K., "The Interaction of a Reflected Shock Wave with the Boundary Layer in a Shock Tube," *Bulletin of JSME*, Vol. 17, No. 110, 1974, pp. 1039–1046. https://doi.org/10.1299/jsme1958.17.1039

[19] Strehlow, R. A., and Cohen, A., "Limitations of the Reflected Shock Technique for Studying Fast Chemical Reactions and Its Application to the Observation of Relaxation in Nitrogen and Oxygen," *The Journal of Chemical Physics*, Vol. 30, No. 1, 1959, pp. 257–265. https://doi.org/10.1063/1.1729883

[20] Hargis, J. W., and Petersen, E. L., "Methane Ignition in a Shock Tube with High Levels of CO_2 Dilution: Consideration of the Reflected-Shock Bifurcation," *Energy & Fuels*, Vol. 29, No. 11, 2015, pp. 7712–7726. https://doi.org/10.1021/acs.energyfuels.5b01760

[21] Kleine, H., Lyakhov, V. N., Gvozdeva, L. G., and Grönig, H., "Bifurcation of a Reflected Shock Wave in a Shock Tube," Berlin, Heidelberg, 1992. https://doi.org/10.1007/978-3-642-77648-9_36

[22] Sanderson, R. J., "Interpretation of Pressure Measurements behind the Reflected Shock in a Rectangular Shock Tube.," *AIAA Journal*, Vol. 7, No. 7, 1969, pp. 1370–1372. https://doi.org/10.2514/3.5352

[23] Wilson, G., Sharma, S., and Gillespie, W., "Time-Dependent Simulation of Reflected-Shock/Boundary Layer Interaction," presented at the 31st Aerospace Sciences Meeting, Reno,NV,U.S.A., 1993. https://doi.org/10.2514/6.1993-480

[24] Trolier, J. W., and Duffy, R. E., "Turbulence Measurements in Shock-Induced Flows," *AIAA Journal*, Vol. 23, No. 8, 1985, pp. 1172–1178. https://doi.org/10.2514/3.9060

[25] Keller, J., and Merzkirch, W., "Interaction of a Normal Shock Wave with a Compressible Turbulent Flow," *Experiments in Fluids*, Vol. 8, No. 5, 1990, pp. 241–248. https://doi.org/10.1007/BF00187225

[26] Hartunian, R. A., Russo, A. L., and Marrone, P. V., "Boundary-Layer Transition and Heat Transfer in Shock Tubes," *Journal of the Aerospace Sciences*, Vol. 27, No. 8, 1960, pp. 587–594. https://doi.org/10.2514/8.8656

[27] Svete, A., and Kutin, J., "Diaphragmless Shock Tube for Primary Dynamic Calibration of Pressure Meters," *Acta IMEKO*, Vol. 9, No. 5, 2020, pp. 310–314. https://doi.org/10.21014/acta_imeko.v9i5.990

[28] Hong, Z., Pang, G. A., Vasu, S. S., Davidson, D. F., and Hanson, R. K., "The Use of Driver Inserts to Reduce Non-Ideal Pressure Variations behind Reflected Shock Waves," *Shock Waves*, Vol. 19, No. 2, 2009, pp. 113–123. https://doi.org/10.1007/s00193-009-0205-y

[29] Handa, T., Masuda, M., and Matsuo, K., "Three-Dimensional Normal Shock-Wave/Boundary-Layer Interaction in a Rectangular Duct," *AIAA Journal*, Vol. 43, No. 10, 2005, pp. 2182–2187. https://doi.org/10.2514/1.12976

[30] Alpher, R. A., and White, D. R., "Flow in Shock Tubes with Area Change at the Diaphragm Section," *Journal of Fluid Mechanics*, Vol. 3, No. 05, 1958, p. 457. https://doi.org/10.1017/S0022112058000124

[31] Amer, E., Wozniak, M., Jönsson, G., and Arrhén, F., "Evaluation of Shock Tube Retrofitted with Fast-Opening Valve for Dynamic Pressure Calibration," *Sensors*, Vol. 21, No. 13, 2021, p. 4470. https://doi.org/10.3390/s21134470

[32] Shumway, N., and Laurence, S. J., "Methods for Identifying Key Features in Schlieren Images from Hypersonic Boundary-Layer Instability Experiments," presented at the 53rd AIAA Aerospace Sciences Meeting, Kissimmee, Florida, 2015. https://doi.org/10.2514/6.2015-1787

[33] Weber, Y. S., Oran, E. S., Boris, J. P., and Anderson, J. D., "The Numerical Simulation of Shock Bifurcation near the End Wall of a Shock Tube," *Physics of Fluids*, Vol. 7, No. 10, 1995, pp. 2475–2488. https://doi.org/10.1063/1.868691

[34] MIRELS, H., "Shock Tube Test Time Limitation Due to Turbulentwall Boundary Layer," *AIAA Journal*, Vol. 2, No. 1, 1964, pp. 84–93. https://doi.org/10.2514/3.2218

[35] Welch, P., "The Use of Fast Fourier Transform for the Estimation of Power Spectra: A Method Based on Time Averaging over Short, Modified Periodograms," *IEEE Transactions on Audio and Electroacoustics*, Vol. 15, No. 2, 1967, pp. 70–73. https://doi.org/10.1109/TAU.1967.1161901

[36] Ozawa, H., "Experimental Study of Unsteady Aerothermodynamic Phenomena on Shock-Tube Wall Using Fast-Response Temperature-Sensitive Paints," *Physics of Fluids*, Vol. 28, No. 4, 2016, p. 046103. https://doi.org/10.1063/1.4947040

[37] "Sutherland's Law." Retrieved 19 July 2024. https://doc.comsol.com/5.5/doc/com.comsol.help.cfd/cfd_ug_fluidflow_high_mach.08.27.html

APPENDIX A.

Sample calculations of M_s and Re_2 (based on Test Condition 6).

For this test condition, the desired shock Mach number M_s was 2.2 and the driver and driven pressures P_4 and P_1 were 550 kPa and 4 kPa, respectively. At this time, the room temperature was 25.4°C. Air was used as the driven gas, and had a specific gas constant R_1 of 287.1 J/kg·K and ratio of specific heats γ_1 of 1.4. These initial conditions are shown as

$$P_4 = 550\ \text{kPa}, \quad P_1 = 4\ \text{kPa}$$

$$T_4 = T_1 = 25.4\ \text{°C} = 298.5\ \text{K}$$

$$R_1 = 287.1\ \text{J/(kg·K)}, \quad \gamma_1 = 1.4$$

The speed of sound in region 1 a_1 can be calculated using the initial conditions:

$$a_1 = \sqrt{\gamma_1 R_1 T_1} = \sqrt{(1.4)(287.1)(298.5)} = 346\ \text{m/s}.$$

The center-to-center distances between PCB 1 and PCB 2 was measured to be 73 mm prior to the experiment.

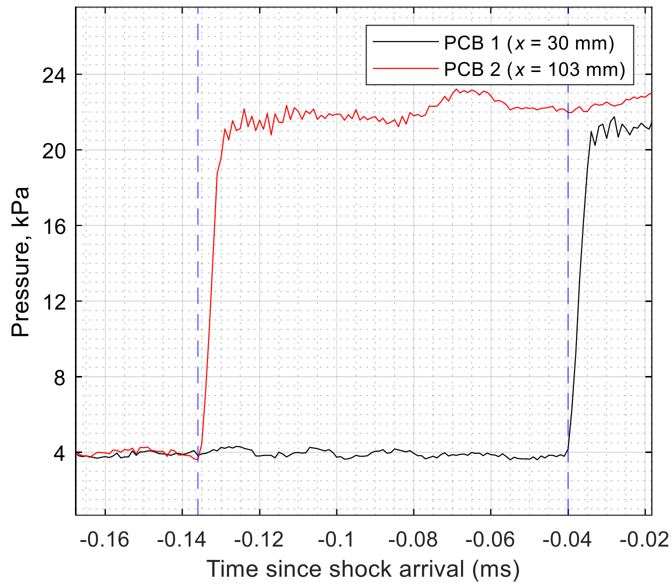

Figure A1.1: Pressure histories recorded by PCB 1 and PCB 2 for Test Condition 6, shot #1.

After performing the experiment and performing data analysis, the following pressure records were obtained from PCB 1 and PCB 2 and are shown in Figure A1.1. The time in between the pressure rise at both sensors is 96 μs as indicated by the blue dashed lines in the figure. The distance between the two sensors is 73 mm; the shock speed u_s can be subsequently calculated by

$$u_s = \frac{x}{t} = \frac{0.073}{0.000096} = 760\ \mathrm{m/s}.$$

The shock Mach number is subsequently found by

$$M_s = \frac{u_s}{a_1} = \frac{760}{346} = 2.20.$$

To determine the freestream Reynolds number, the following procedure was performed. The temperature in region 2 T_2 was found by

$$T_2 = T_1\left(1 + \frac{2\gamma_1}{\gamma_1 + 1}(M_s^2 - 1)\right)\frac{(2 + (\gamma_1 - 1)M_s^2)}{(\gamma_1 + 1)M_s^2}$$

and was used to calculate the dynamic viscosity of the gas in region 2 μ_2 using the Sutherland equation:

$$\mu_2 = \frac{\mu_0(T_0 + S)}{T_2 + S}\left(\frac{T_2}{T_0}\right)^{\frac{3}{2}}.$$

In this case, the parameters μ_0, T_0, and S are parameters specific to the gas being tested; in this case, the gas is standard air, so $\mu_0 = 1.716\ \mathrm{N{\cdot}s/m^2}$, $T_0 = 273.15$ K, and $S = 110$ K [37].

The solution to these two equations are shown below:

$$T_2 = 298.5 \cdot \left(1 + \frac{(2 \cdot 1.4)}{1.4 + 1} \cdot (2.20^2 - 1)\right) \cdot \frac{2 + (1.4 - 1) \cdot 2.20^2}{(1.4 + 1) \cdot 2.20^2} = 698\ \mathrm{K}$$

$$\mu_2 = (1.716 \times 10^{-5}) \cdot \frac{273.15 + 110}{698 + 110} \cdot \left(\frac{698}{273.15}\right) = 2.86 \times 10^{-5}\ \mathrm{N{\cdot}s/m^2}$$

The freestream velocity in region 2 must now be determined using the Rankine-Hugoniot relations:

$$u_2 = \frac{2\sqrt{\gamma_1 R_1 T_1}}{\gamma_1 + 1}\frac{M_s^2 - 1}{M_s^2} = 2 \cdot \frac{\sqrt{1.4 \cdot 287.1 \cdot 298.5}}{1.4 + 1}\frac{2.20^2 + 1}{2.20^2} = 504\ \mathrm{m/s}$$

The density in region 2 is determined through use of the normal shock relations combined with perfect gas law:

$$\rho_2 = \frac{P_1}{R_1 T_1}\frac{(\gamma_1 + 1)M_s^2}{(\gamma_1 - 1)M_s^2 + 2} = \frac{4}{287.1 \cdot 298.5} \cdot \frac{(1.4 + 1) \cdot 2.20^2}{(1.4 - 1) \cdot 2.20^2 + 2} = 0.138\ \mathrm{kg/m^3}$$

With the density, velocity, and viscosity in the region 2 now found, the freestream unit Reynolds number in region 2 can be found:

$$Re_2 = \frac{\rho_2 u_2}{\mu_2} = \frac{0.138 \cdot 504}{2.86 \times 10^{-5}} = 2.43 \times 10^6 \text{ 1/m} \therefore$$

This procedure was repeated for each individual experiment that was performed within the thesis.

APPENDIX B.

Summarization of Mirels' laminar boundary layer solutions behind a shockwave along a flat plate

Mirels' approach to the laminar boundary layer thickness approximation utilizes the similarity parameters first set forth by Blasius' original solutions for the incompressible boundary layer on a flat plate. Mirels modified the boundary conditions used in Blasius' differential equation, and additionally accounted for the temperature changes that are present within a boundary layer formed at elevated velocities.

The similarity parameter η is defined as

$$\eta = \sqrt{\frac{1}{2}\frac{u_e}{x\nu_w}}\int_0^y \frac{T_w}{T}\,\mathrm{d}y$$

where

$$u_e = u_s - u_2, \quad u_w = u_s$$

and

$$\nu_w = \frac{\mu_w}{\rho_w} \approx \frac{\mu_1}{\rho_1}.$$

The wall temperature is assumed to be insulated in this case, and can be found by

$$T_{w,i} = T_e\left(1 + \frac{\gamma_1 - 1}{2}\left(\left(\frac{u_w}{u_e} - 1\right)M_e\right)^2 r(0)\right),$$

where

$$T_e = T_2$$

and

$$M_e = \frac{u_e}{a_2}.$$

The temperature distribution within the boundary layer can be found by

$$T = T_e\left(1 + \frac{\gamma_1 - 1}{2}\left(\left(\frac{u_w}{u_e} - 1\right)M_e\right)^2 r(\eta) + \left(\left(\frac{T_w}{T_e} - \frac{T_{w,i}}{T_e}\right)s(\eta)\right)\right).$$

The recovery factory $r(\eta)$ and parameter $s(\eta)$ are found through solutions to the Blasius differential equation using the similarity function $f(\eta)$:

$$f''' + ff'' = 0$$

$$\text{Boundary Conditions: } f(0) = 0,\ f'(0) = \frac{u_w}{u_e}, f'(\infty) = 1$$

$$r'' + \sigma f r' = -\frac{2\sigma}{\left(\frac{u_w}{u_e} - 1\right)^2} f''^2$$

$$\text{Boundary Conditions: } r(\infty) = 0, r'(0) = 0$$

$$s" + \sigma f s' = 0$$

$$\text{Boundary Conditions: } s(0) = 1,\ s(\infty) = 0$$

The Prandtl number, σ, is assumed to equal 0.72 for this case, as air is the test gas. The value of η corresponding to a 95% boundary layer thickness can be found where $\frac{\frac{u_w}{u_e} - f'(\eta)}{\frac{u_w}{u_e} - 1} \geq$

0.95. At this value of η, the boundary layer thickness at a distance x from the endwall can be found by

$$\delta(x) = \left(\frac{\frac{1}{2}u_e}{x\nu_w}\right)^{-1/2} \int_0^\eta \frac{T}{T_w}\,\mathrm{d}\eta$$

Therefore, as long as the temperature distribution with respect to η and the value of η that corresponds to the desired boundary layer thickness percentage can be approximated, the boundary layer thickness at a specific distance x can be found. Using the velocity relation $x = u_s t$, the boundary layer thickness variation over time can be determined.

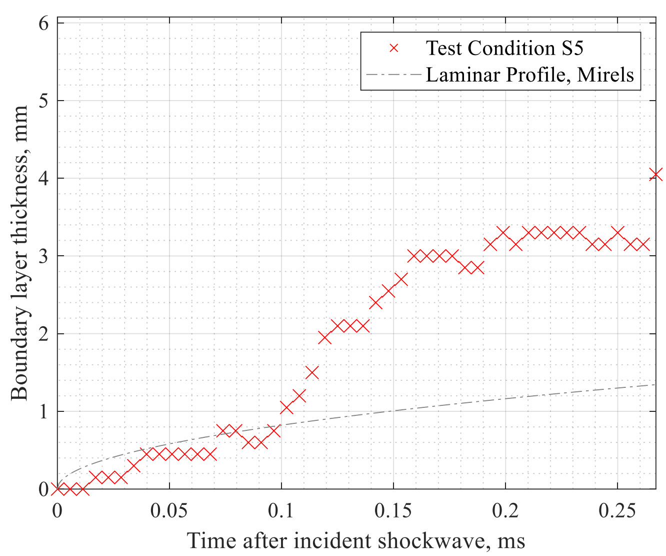

Figure A2.1. Comparison between boundary layer profile extracted in Test Condition S5 and the equivalent laminar boundary layer profile calculated by Mirels' laminar theory.

A comparison between this theoretical method and the experimental technique used within the thesis can be seen in Figure A2.1. The laminar portion of the experimental boundary layer reflects a similar trend to the theoretical profile, though a slight discrepancy between the two profiles is observed. This is likely due to inaccuracies in the boundary layer extraction technique as well as the assumption that the wall is insulated.